Combined ADAMTS10 and ADAMTS17 inactivation exacerbates bone shortening and compromises extracellular matrix formation

Nandaraj Taye[1,‡], Stylianos Z. Karoulias[1,*,‡], Zerina Balic[1,**], Lauren W. Wang[3,4], Belinda B. Willard[2], Daniel Martin[3], Daniel Richard[5], Alexander S. Okamoto[5], Terence D. Capellini[5,6], Suneel S. Apte[3,4] & Dirk Hubmacher[1,7,***]

[1]Orthopedic Research Laboratories, Leni & Peter W. May Department of Orthopedics, Icahn School of Medicine at Mount Sinai, New York, NY, 10029, USA

[2]Proteomics and Metabolomics Core, Cleveland Clinic Lerner Research Institute, Cleveland, OH, 44195, USA.

[3]Department of Biomedical Engineering, Cleveland Clinic Lerner Research Institute, Cleveland, OH, 44195, USA

[4]Department of Orthopaedic Surgery, Cleveland Clinic Orthopaedic and Rheumatologic Institute, Cleveland, OH, 44195, USA

[5]Human Evolutionary Biology, Harvard University, Cambridge, MA, 02138, USA

[6]Broad Institute of MIT and Harvard, Cambridge, MA, 02142, USA

[7]Mindich Child Health and Development Institute, Icahn School of Medicine at Mount Sinai, New York, NY, 10029, USA

[*]Current affiliation: Regeneron Pharmaceuticals, Tarrytown, NY, 10591, USA

[**]Current affiliation: Weill Cornell BCMB program, Sloan Kettering Institute, New York, NY, 10065, USA

[***]Corresponding author: dirk.hubmacher@mssm.edu

[‡]These authors contributed equally.

Running title: ADAMTS10 and ADAMTS17 regulate bone growth

Key words: Extracellular matrix, Weill Marchesani syndrome, ADAMTS proteases, fibrillin, short stature syndromes

Abstract

Weill-Marchesani syndrome (WMS) is characterized by severe short stature, short hands and feet (brachydactyly), joint contractures, tight skin, and heart valve, eye, and skin anomalies. Whereas recessive WMS is caused by mutations in *ADAMTS10*, *ADAMTS17*, or *LTBP2*, dominant WMS is caused by mutations in *FBN1* (encoding fibrillin-1). Since bone growth is driven by chondrocyte proliferation and hypertrophy in the growth plates, the genetics of WMS suggests that the affected ECM proteins act within the same pathway to regulate chondrocyte and growth plate function. Here, we investigated the role of the secreted ADAMTS proteases ADAMTS10 and ADAMTS17 in growth plate function and ECM formation. We generated *Adamts10*;*Adamts17* double knockout (DKO) mice, which showed significant postnatal lethality compared to single *Adamts10* or *Adamts17* KO mice. Importantly, we observed severe bone shortening DKO mice, which correlated with a narrower hypertrophic zone in their growth plates. ADAMTS17 substrates identified by N-terminomics and yeast two-hybrid screening identified the ECM proteins fibronectin and collagen VI (COL6). However, validation experiments did not reveal direct proteolysis of either fibronectin or COL6 by ADAMTS17. We then investigated ECM formation in primary ADAMTS10- and ADAMTS17-deficient skin fibroblasts and observed compromised fibronectin deposition concomitant with aberrant intracellular accumulation of fibrillin-1. These findings support a role for ADAMTS17 in ECM protein secretion and assembly. Collectively, our data suggest that ADAMTS10 and ADAMTS17 regulate bone growth by regulating chondrocyte hypertrophy or hypertrophic chondrocyte turnover. Mechanistically, ADAMTS17 appears to be a critical regulator of ECM protein secretion or pericellular matrix assembly, whereas ADAMTS10 likely modulates ECM formation at later stages, possibly regulating the spatio-temporal deposition of fibrillin isoforms.

Introduction

Acromelic dysplasias are a group of genetic conditions resulting in severe short stature and shortening of distal limb elements[1,2]. Among them, Weill-Marchesani syndrome (WMS) has been characterized genetically resulting from mutations in distinct, but functionally related genes, encoding extracellular matrix (ECM) proteins[1,3]. Recessive pathogenic variants in secreted ADAMTS10 cause Weill-Marchesani syndrome 1 (WMS1)[4-6]. Distinct WMS sub-types can also be caused by dominant mutations in fibrillin-1 (*FBN1*, WMS2) or recessive mutations in *LTBP2* (WMS3) or *ADAMTS17* (WMS4) suggesting that these four genes may act together in pathways that regulate development and homeostasis of affected tissues[4,7-11]. WMS is characterized by short stature, lens dislocation, microspherophakia and other eye anomalies, progressive joint stiffness, and tight skin[3,12]. Lens dislocation and/or changes in the outflow track can block the drainage of aqueous humor from the anterior chamber of the eye and cause glaucoma in WMS. WMS1 also has cardiovascular manifestations such as patent ductus arteriosus, pulmonary valve dysplasia, which can lead to pulmonary stenosis, and in rare cases aortic aneurysms[6,8,12]. In dogs, mutations in *ADAMTS10* and *ADAMTS17* were associated with primary open angle glaucoma[13-17]. Homozygosity of a glaucoma-causing canine *ADAMTS17* variants was also associated with short stature in several dog breeds[18]. WMS-causing ADAMTS10 and ADAMTS17 mutations are distributed over the entire molecule and result in loss-of-function or haploinsufficiency due to impaired secretion[1,3,10,11]. The fact that mutations in *ADAMTS10* and *ADAMTS17* each cause WMS suggests that these genes cooperate, have superimposed mechanisms, or act in the same pathways that regulate the development or homeostasis of affected tissues, including the growth plate, which drives bone growth, the skin, and the eye[19,20]. ADAMTS10 and ADAMTS17 each bind to fibrillin-1, which may provide a scaffold for their tissue-specific deposition or functional regulation[21,22]. In addition, ADAMTS10 was shown to promote the assembly of fibrillin-1 in cell culture[21].

The 19 ADAMTS proteases are involved in diverse biological processes including tissue morphogenesis and homeostasis[23,24]. Mutations in several ADAMTS proteases cause birth defects and inherited connective tissue disorders in humans and other species[25]. In addition, ADAMTS proteases contribute to the progression of acquired disease, such as the aggrecanase ADAMTS5 in osteoarthritis[26]. These diverse roles are attributed to the actions of ADAMTS proteases on distinct substrates. Recognized ECM substrates for ADAMTS proteases include proteoglycans such as aggrecan and versican, the ECM

scaffolding proteins fibrillin-1, fibrillin-2, and fibronectin, and several collagens[23]. Most ADAMTS proteases are secreted as inactive zymogens whose activation requires proteolytic removal of their prodomains by furin or other proprotein convertases[27-30]. ADAMTS10, however, lacks a canonical furin recognition site and is poorly processed by furin. Consistent with poor furin-processing, ADAMTS10 appears to be an inefficient protease, although, once activated by mutagenesis to restore a canonical furin-processing site, ADAMTS10 could cleave fibrillin-1 and fibrillin-2 in vitro[21,31]. However, alternative furin-independent mechanisms of ADAMTS10 activation in vitro or in vivo remain elusive. ADAMTS17 is secreted as an active protease, but fragments itself extensively and efficiently, including within the catalytic domain, prior to its release from the surface of HEK293 cells[22]. These findings suggested that ADAMTS17 may act as a protease in the secretory pathway or at the cell surface. ADAMTS17 substrates other than itself have not been identified. We showed previously that ADAMTS17 interacted with fibrillin-1 and fibrillin-2 but did not cleave either[22,32].

Adamts10 and *Adamts17* inactivation in mice was previously reported with differential phenotypes. While *Adamts10* knockout (KO) mice did not result in short stature, *Adamts17* KO mice had shorter bones and growth plate abnormalities[31,33]. Interestingly, the knock-in of a WMS mutation into the mouse *Adamts10* locus resulted in short stature and growth plate abnormalities[34]. In addition, knock-in of an *ADAMTS10* mutation that causes glaucoma in dogs into the mouse *Adamts10* locus also resulted in short stature[35]. Together, these findings support a role for ADAMTS10 and ADAMTS17 in regulating bone growth and thus height. If and how ADAMTS10 and ADAMTS17 cooperate in regulating bone growth and in the formation and maintenance of other tissues affected in WMS is not known. Here, we investigated the genetic interactions of ADAMTS10 and ADAMTS17 by analyzing the bone and skin phenotypes of *Adamts10*;*Adamts17* double KO (DKO) mice. For insights on molecular mechanisms, we evaluated potential ADAMTS17 substrates and binding partners identified by N-terminomics and yeast two-hybrid screening, respectively. The findings of our studies, taken together with prior work strongly suggest a cooperative role for these proteases in skeletal growth and provide a putative molecular basis for their ECM-regulatory activities.

Results

Combined *Adamts10* and *Adamts17* inactivation resulted in early postnatal mortality and reduced body size.

To generate *Adamts10;Adamts17* DKO mice, we combined a previously published *Adamts10* KO allele with a novel *Adamts17* KO allele. The *Adamts10* KO allele was generated by replacing 41 bp of *Adamts10* exon 5 with an IRES-*lacZ-neo* cassette[31]. The *Adamts17* KO allele was generated using CRISPR/Cas9-induced non-homologous end-joining with guide RNAs targeting *Adamts17* exon 3 (Fig. 1A). The resulting dinucleotide insertion (AT) in exon 3 of *Adamts17* (*Adamts17* 670_671insAT, NM_001033877.4) caused a reading frame shift (p.I190fsX12), which resulted in a premature termination codon presumed to trigger nonsense-mediated mRNA decay (Fig. 1A). The AT insertion in *Adamts17* was verified by Sanger sequencing of a PCR product amplified from template DNA isolated from toe tissue with *Adamts17*-specific primers flanking exon 3 (Fig. 1B). Mice homozygous for the *Adamts17* AT insertion are referred to as *Adamts17* KO. Loss of ADAMTS17 protein was validated by immunostaining tissue and primary skin fibroblasts isolated from wild type (WT) and *Adamts17* KO mice using a monoclonal ADAMTS17 antibody. In sections through WT skin and the tibial growth plate, ADAMTS17 immunoreactivity was apparent around hair follicles and in hypertrophic chondrocytes, respectively. This signal was absent or strongly reduced in comparable sections from *Adamts17* KO or *Adamts10;Adamts17* DKO mice (Fig. 1C). In primary WT skin fibroblasts, the ADAMTS17 signal was most intense in perinuclear regions, where the endoplasmic reticulum and Golgi are located, and in patches between cells (Fig. 1C, right). Similar to tissue sections, the ADAMTS17 signal was absent in DKO fibroblasts. Thus, genetic inactivation of ADAMTS17 eliminated ADAMTS17 protein in relevant tissues and primary cells and at the same time validated the specificity of the monoclonal ADAMTS17 antibody.

Adamts17 KO mice were born at the expected Mendelian ratio and were viable (Fig. 1D). To generate DKO mice, we first crossbred *Adamts10* Het and *Adamts17* Het mice to generate *Adamts10;Adamts17* double-heterozygous mice (Fig. 1E). *Adamts10* Het;*Adamts17* Het mice were then intercrossed to generate offspring with all allelic combinations, among which WT, *Adamts10* KO; *Adamts17* KO, and

Adamts10;*Adamts17* DKO mice were the focus of subsequent analyses. In principle, this breeding scheme allows comparison of the phenotypes from littermates. However, due to the low predicted percentages for WT and DKO mice (6.25%) per litter in these crosses, we also intercrossed *Adamts10* Het or *Adamts17* Het mice to generate the respective WT and individual KOs as age- and sex-matched controls for DKO mice. We first analyzed the *Adamts10* and *Adamts17* genotype distribution of 180 mice at postnatal day (P) 7-P10 and determined statistically significant deviations from the expected Mendelian ratios using Chi^2 calculation (Fig. 1F). *Adamts17* KO (3.9% vs. 6.25 expected), *Adamts10* KO;*Adamts17* Het (6.7% vs 12.5% expected), and DKO (3.9% vs. 6.25 expected) mice were present in significantly lower numbers than expected and the percentage of *Adamts10*;*Adamts17* double heterozygous mice was significantly higher (34.4% vs. 25% expected). This resulted in a Chi^2 value of 18.09 (8 degrees of freedom) and a p-value of <0.05, suggesting reduced viability or embryonic lethality due to reduced *Adamts17* gene dosage or the combined absence of *Adamts10* and *Adamts17*. Since we observed early postnatal lethality of *Adamts10*;*Adamts17* DKO mice, we quantified postnatal survival with Kaplan-Meier survival analysis, where we observed significant postnatal mortality of DKO mice with 50% survival at 23 d (+/-7.1 d) after birth (probe > Chi^2 = 0.00029, log-rank test) (Fig. 1G). The cause of death is unknown. In addition to reduced survival of DKO mice, we noted reduced body size, which correlated with several genotypes, most notably *Adamts17* KO mice, *Adamts10* KO;*Adamts17* Het mice and DKO mice (Fig. 1H). These size differences were also apparent from body weight measurements at 4 weeks of age where the weights of *Adamts10* KO;*Adamts17* Het and DKO mice were significantly reduced compared to WT (Fig. 1I). However, after normalization of the body weight to the average femur lengths, these differences became non-significant, suggesting proportionate short stature (Fig. 1J).

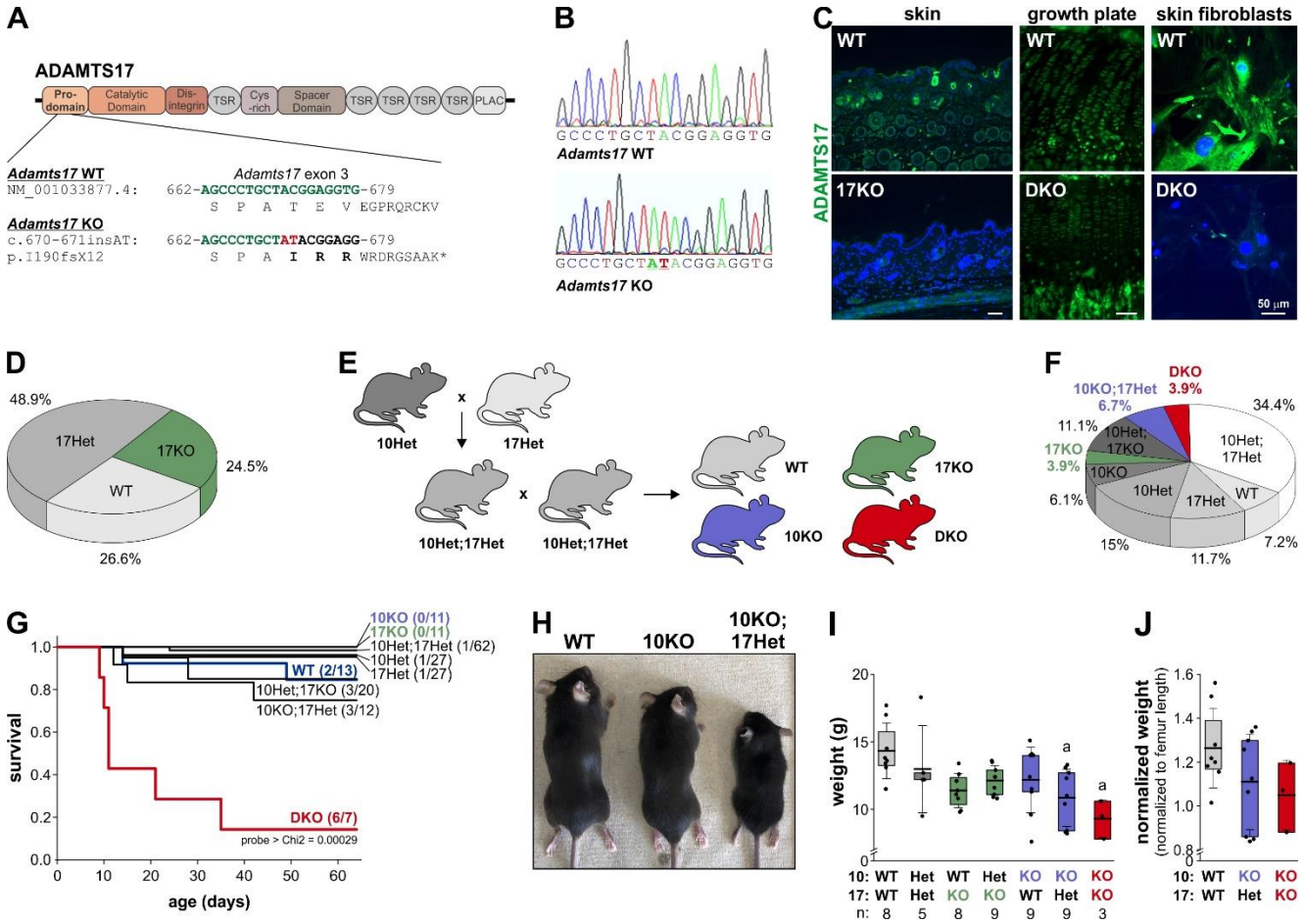

Figure 1. Generation of Adamts17 KO and Adamts10;Adamts17 DKO mice. A) *Domain organization of ADAMTS17 shows location and targeting of exon 3 by CRISPR/Cas9 gRNA to induce non-homologous end joining. The nucleotide and amino acid sequence of the ADAMTS17 WT allele (green) and after AT insertion (red) are indicated. The dinucleotide insertion induced a frameshift, which resulted in a premature stop codon after 12 amino acids.* ***B)*** *Sanger sequencing traces of a PCR product generated with primers flanking exon 3 showing the AT insertion (underlined) in the Adamts17 KO.* ***C)*** *Micrographs of ADAMTS17 immunostaining of sections through WT and Adamts17 KO skin (left), DKO growth plates (middle), and of primary DKO mouse skin fibroblasts (right). The signal in the dermis around hair follicles, in growth plate chondrocytes, and in fibroblasts and their ECM originating from the monoclonal ADAMTS17 antibody was strongly reduced in KO and DKO tissues and cells, indicating lack of ADAMTS17 protein in Adamts17 KO mice.* ***D)*** *Pie chart showing Mendelian distribution of genotypes recovered from Adamts17 Het intercrosses at the time of genotyping (P7-P10) (n=94 mice).* ***E)*** *Breeding scheme to generate WT, Adamts10 KO (10KO), Adamts17 KO (17KO), and DKO mice.* ***F)*** *Pie chart*

showing distribution of genotypes recovered from Adamts10 Het;Adamts17 Het intercrosses at P7-P10 (n=180 mice). Statistical analysis was performed using Chi square calculation. ***G)*** *Kaplan-Meier survival analysis of DKO mice. The numbers of observed dead/total mice for the individual genotypes are indicated in brackets. Statistical significance was determined using a log-rank test.* ***H)*** *Whole mount images of WT, 10KO, 10KO;17Het mice at 4 weeks of age shows progressive reduction in body size.* ***I)*** *Bar graphs showing body weights of 4-week-old mice of the indicated genotypes. The number of mice is indicated below the genotypes.* ***J)*** *Bar graphs showing body weight normalized to average femur length for the genotypes that were significantly different in I. In I, J floating bars indicate the 25th – 75th percentile range, lines the mean value, and whiskers the standard deviation. Statistical differences in I, J were determined using a one-way ANOVA with post-hoc Tukey test. a, p<0.05 compared to WT.*

Combined *Adamts10;Adamts17* depletion exacerbated bone shortening.

To determine if *Adamts10* and *Adamts17* gene dosage affected bone length, we quantified the lengths of forelimb and hind limb bones from X-ray images taken at 4 weeks of age (Fig. 2A-L). Overall, *Adamts10*;*Adamts17* DKO mice had the shortest bones across all genotypes when compared to WT or individual KOs. In addition, *Adamts17* KO bones were significantly shorter than WT, except for the humerus, the 1st metacarpal, and the 1st metatarsal. Notably, deletion of one *Adamts17* allele in *Adamts10* KO mice exacerbated bone shortening, but not vice versa, except in the fibula, the 1st metacarpal, and the 1st metatarsal. The lengths of the 1st metacarpal and 1st metatarsal were significantly shorter in DKO mice compared to WT, *Adamts10* KO, and *Adamts17* KO but the same bones were not shorter in the individual KOs compared to WT (Fig. 2E, L). The lengths of *Adamts10;Adamts17* double heterozygous bones were not significantly shorter compared to WT bones. Since we previously observed increased bone width in another acromelic dysplasia model (geleophysic dysplasia) due to *Adamtsl2* deficiency, we measured the width of humeri and femora[36]. The mid-shaft width in DKO mice was significantly greater than WT, *Adamts10* KO, or *Adamts17* KO (humerus), or compared to WT (femur) (Fig. 2M, N). In addition, the widths of the *Adamts10* KO;*Adamts17* Het humerus and femur were increased compared to WT, but not the individual KOs. Collectively, combined inactivation of ADAMTS10 and ADAMST17 exacerbated bone shortening

compared to the individual KOs with *Adamts17* having an apparently stronger gene dosage effect compared to *Adamts10*.

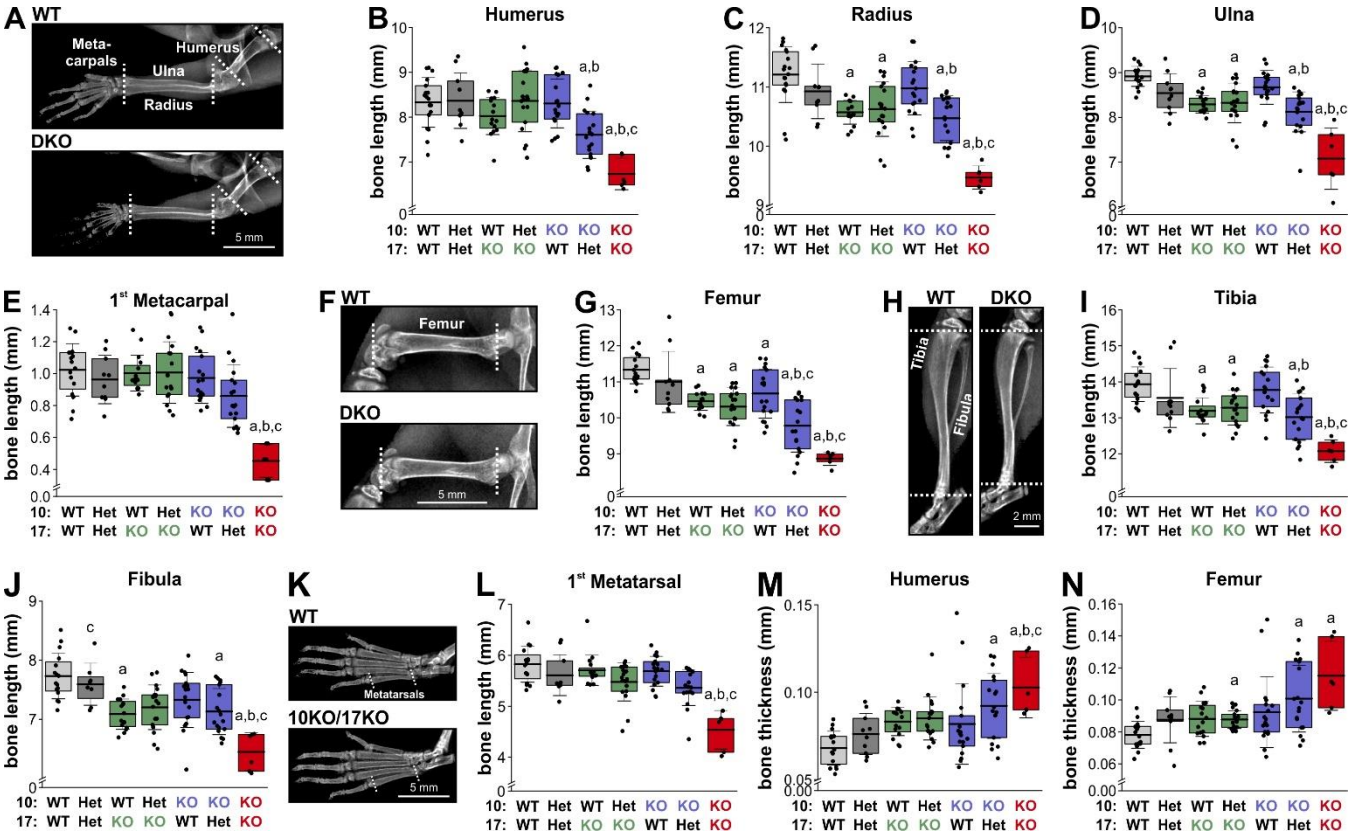

Figure 2. Exacerbated bone shortening in Adamts10;Adamts17 DKO mice. A) *X-ray images showing WT and DKO forelimbs.* ***B-E)*** *Bar graphs showing lengths of humerus (B), radius (C), ulna (D), and 1st metacarpal (E) for all genotypes.* ***F)*** *X-ray images showing WT and DKO femur.* ***G)*** *Bar graphs showing femoral length for all genotypes.* ***H)*** *X-ray images showing WT and DKO tibia and fibula.* ***I, J)*** *Bar graphs showing lengths of tibia (I) and fibula (J) for all genotypes.* ***K)*** *X-ray images showing WT and DKO hind paw bones.* ***L)*** *Bar graphs showing length of 1st metatarsal for all genotypes.* ***M, N)*** *Bar graphs showing thickness of humerus (M) and femur (N) at mid-shaft. For number of mice see Fig. 1I. All mice were 4 weeks old at the time of X-ray imaging. Bones from both limbs were measured and measurement from male and female mice were combined. In B, C, D, E, G, I, J, L, M, N floating bars indicate the 25th – 75th percentile range, lines the mean value and whiskers the standard deviation. Statistical differences in B,*

C, D, E, G, I, J, L, M, N were determined using a one-way ANOVA with post-hoc Tukey test. a, p<0.05 compared to WT; b, p<0.05 compared to Adamts10 KO; c, p<0.05 compared to Adamts17 KO.

Combined *Adamts10* and *Adamts17* inactivation compromised growth plate chondrocyte function.

Since bone growth is largely driven by growth plate activity, i.e. the proliferation and hypertrophic expansion of growth plate chondrocytes, we quantified growth plate dimensions and primary chondrocyte behavior in ADAMTS10 and ADAMTS17 deficient tissue and chondrocytes[37,38]. Compared to WT growth plates, DKO growth plates showed a narrower hypertrophic zone, while the proliferative zone was unchanged (Fig. 3A, B). In addition, the columnar organization of proliferating chondrocytes appeared to be irregular with more spacing between chondrocyte columns (Fig. 3C). By immunostaining, we localized ADAMTS17 in the pericellular matrix of hypertrophic chondrocytes in wild type growth plates, close to the cartilage-bone interface (Fig. 3D). These data suggested that ADAMTS17 could play a role in regulating or maintaining chondrocyte hypertrophy. Therefore, we next used high cell density pellet cultures of mouse embryo CH3/10T1/2 cells to model chondrocyte-like differentiation in vitro and to determine the temporal dynamics of *Adamts10* and *Adamts17* mRNA expression during chondrocyte maturation in vitro by quantitative real-time (qRT)-PCR (Fig. 3E). *Adamts10* mRNA levels significantly decreased between 0 and 2 days after induction of differentiation and remained low thereafter (Fig. 3F). In contrast, *Adamts17* mRNA levels started to moderately increase until 7 days after induction of differentiation followed by a strong and statistically significant increase at 10 days. This suggested downregulation of *Adamts10* and induction of *Adamts17* gene expression during in vitro chondrogenesis of CH3/10T1/2 pellet cultures. The strong reduction of *Col2a1* mRNA levels between 0 and 2 days after induction of differentiation was consistent with CH3/10T1/2 pellet cultures undergoing differentiation.

To further probe the regulation of *Adamts10* and *Adamts17* expression during chondrocyte hypertrophy, we treated primary WT rib chondrocytes with okadaic acid, a protein phosphatase 2A inhibitor, which results in de-repression of chondrocyte hypertrophy genes (Fig. 3G)[39,40]. qRT-PCR showed significant upregulation of *Adamts10* and *Adamts17* mRNA levels 24 h after treatment of primary WT chondrocytes with okadaic acid compared to DMSO-treated control chondrocytes (Fig.

3H). Increased *Col10a1* mRNA levels, a marker for hypertrophic chondrocytes, served as a positive control for okadaic acid-mediated de-repression of chondrocyte hypertrophy genes. In addition to *Adamts10* and *Adamts17*, mRNAs for genes encoding the ECM proteins fibrillin-1 (*Fbn1*) and fibronectin (*Fn1*) were also induced. Fibrillin-1 binds to ADAMTS10 and ADAMTS17 and mutations in *FBN1* cause WMS2[9,21,22]. Fibronectin forms the ECM scaffold required for fibrillin-1 deposition in the ECM of mesenchymal cells[41]. Using immunostaining, we confirmed increased fibrillin-1 and fibronectin ECM deposition in primary WT chondrocytes following okadaic acid treatment (Fig. 3I, J).

Finally, we investigated the implications of ADAMTS10 and ADAMTS17-deficiency on primary rib chondrocyte hypertrophy and the capacity to deposit calcium as hydroxyapatite in their ECM, which is a characteristic of terminal hypertrophic chondrocytes (Fig. 3K). Chondrocytes isolated from *Adamts10* KO ribs showed no difference in alizarin red-positive calcium mineral deposition after 21 d under differentiation and mineralization conditions (Fig. 3L, M). In contrast, calcium mineral deposition by ADAMTS17-deficient primary chondrocytes was significantly reduced, suggesting differential roles or differential compensation for ADAMTS10 and ADAMTS17 in chondrocyte differentiation (Fig. 3N, O).

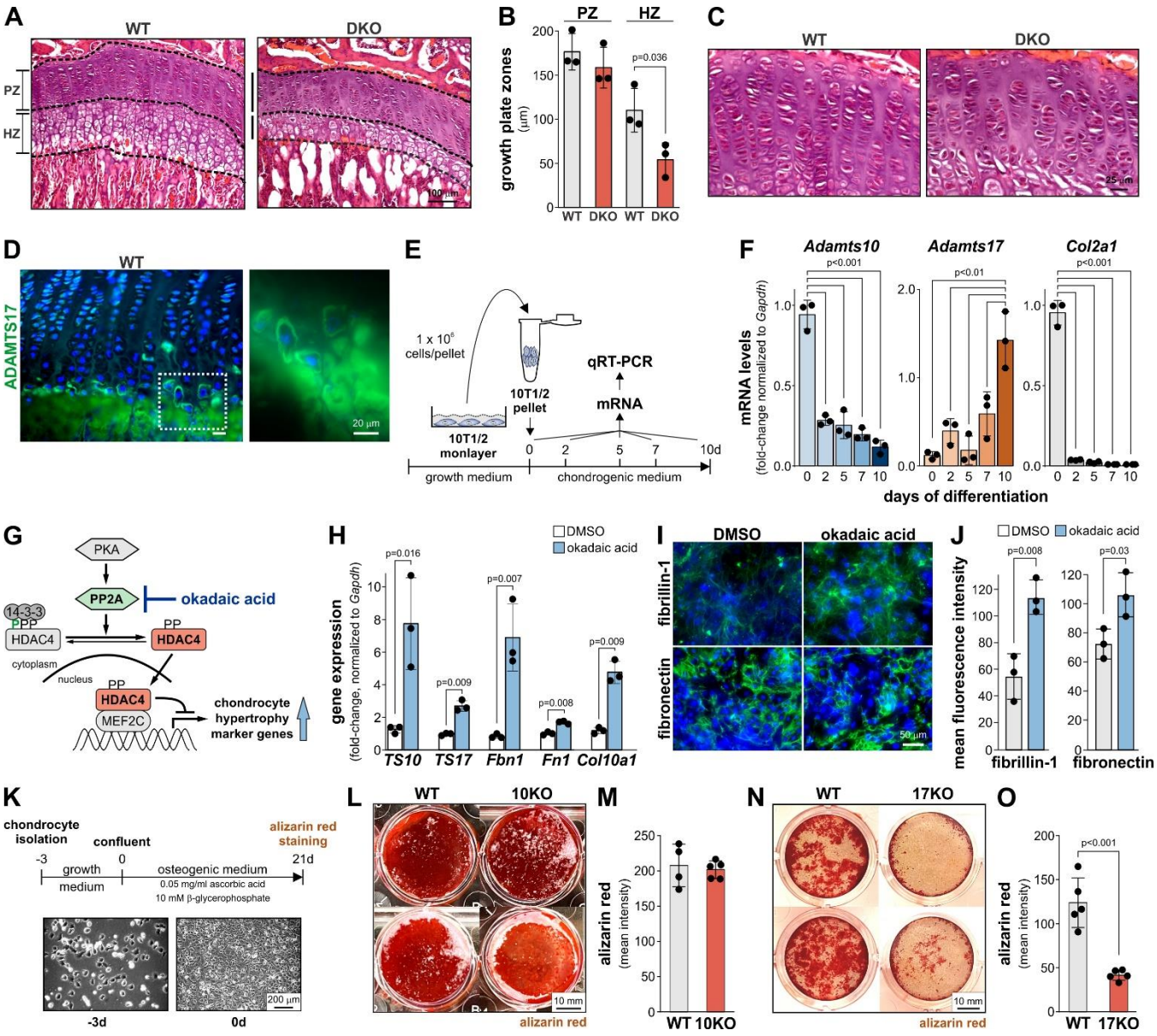

Figure 3. ADAMTS10 and ADAMTS17 regulate growth plate function and chondrocyte hypertrophy. ***A)*** *Images of sections through growth plates of 4 week-old WT and Adamts10;Adamts17 DKO mice. Proliferative (PZ) and hypertrophic (HZ) zones are outlined with dashed lines.* ***B)*** *Bar graphs showing widths of PZ and HZ from WT and DKO growth plates. Data points represent the average of multiple measurements across the growth plate zone from n=3 mice.* ***C)*** *Higher magnification of growth plate from images in A showing disorganized proliferative zone in DKO growth plates.* ***D)*** *Micrograph of ADAMTS17 immunostaining of hypertrophic chondrocytes at the cartilage-bone interface. The boxed*

area is magnified in the right-hand panel. ***E)*** *Schematic representation of experimental design for pellet culture to induce chondrocyte-like differentiation of C3H/10T1/2 cells.* ***F)*** *Bar graphs showing relative Adamts10, Adamts17, and Col2a1 mRNAs levels during differentiation of C3H/10T1/2 cell pellets normalized to Gapdh (n=3 replicates).* ***G)*** *Schematic representation of the mechanism of action of okadaic acid in de-repressing chondrocyte hypertrophy genes.* ***H)*** *Bar graphs showing relative changes of Adamts10 (TS10), Adamts17 (TS17), Fbn1, Fn1, and Col10a1 mRNA levels 24 h after treatment of primary chondrocytes with 50 nM okadaic acid or DMSO (n=3 replicates).* ***I)*** *Micrographs of immunostaining of fibrillin-1 (FBN1) and fibronectin (FN) deposition in the ECM of primary chondrocytes 3 days after treatment with okadaic acid or DMSO only.* ***J)*** *Quantification of mean fluorescence intensity from I (n=3 fields-of-view).* ***K)*** *Schematic representation of osteogenic differentiation of P5 primary rib chondrocytes isolated from Adamts10 KO or Adamts17 KO mice. The bottom panels show brightfield micrographs of freshly isolated primary chondrocytes (-3 d, left) and confluent chondrocytes (0 d, right).* ***L)*** *Micrographs of two individual wells/genotype of primary WT or Adamts10 KO (10KO) chondrocytes stained with alizarin red after 21 d of culture in osteogenic medium.* ***M)*** *Bar graph showing quantification of mean signal intensity of alizarin red deposits (isolates from n=4-5 biological replicates/genotype).* ***N)*** *Micrographs of two individual wells/genotype of primary WT or Adamts17 KO chondrocytes stained with alizarin red after 21 d of culture in osteogenic medium.* ***O)*** *Bar graph showing quantification of mean signal intensity of alizarin red deposits (isolates from n=5 biological replicates/genotype). In B, F, H, J, M, O, bars indicate mean values and whiskers the standard deviation. Statistical significance in B, H, J, M, O was calculated with a 2-sided Student t-test and in F with one-way ANOVA followed by post-hoc Tukey test.*

To gain further insights into the epigenetic and transcriptomic regulation of *ADAMTS10* and *ADAMTS17* during human embryonic development, we data-mined recent assays for transposase-accessible chromatin with sequencing (ATAC-seq) and RNA-transcriptomic data sets, generated from micro-dissected cartilaginous human fetal appendicular skeletal elements (Fig. 4A)[42]. We first identified open chromatin regions by ATAC-seq within +/- 100 kb of *ADAMTS10* and *ADAMTS17* (Fig. 4B, C); each interval containing regulatory elements, such as enhancers, promoters, and repressor sequences, likely drives expression of the nearby gene. For *ADAMTS10*, out of ten total elements within 100 kbp, we

identified three cartilage open chromatin regions that were shared by most or all autopod elements (phalanges, metatarsals and metacarpals), but were absent in stylopod or zeugopod elements, i.e. proximal and distal ends of all major long bones (Fig. 4B, Table 1). One regulatory region was located 100 kb distal to the ADAMTS10 transcription start site (TSS), one overlapping with the final exon, and the other <1 kb proximal to the TSS. We identified two additional cartilage open chromatin regions present in all skeletal elements, located within the *ADAMTS10* gene body. For *ADAMTS17*, we observed a larger number of regulatory elements compared to *ADAMTS10,* consistent with the larger size of *ADAMTS17*. At this locus, 23 cartilage open chromatin regions were identified within or in close vicinity to the *ADAMTS17* gene body (Fig. 4C, Table 2). While three *ADAMTS17* open chromatin regions were identified as accessible in all autopod elements and eight in most, two were specific to individual skeletal elements of the hind limb autopod (metatarsal V). Moreover, in the stylopod and zeugopod elements, two open chromatin regions were shared by the proximal elements but showed mixed accessibility in the corresponding distal ones.

We next analyzed *ADAMTS10* and *ADAMTS17* gene expression in human embryonic skeletal elements by comparing normalized read counts as a measure of ADAMTS10 and ADAMTS17 mRNA abundance (Fig. 4D, E). In stylopodial and zeugopodial elements, normalized read counts for *ADAMTS10* were generally higher compared to *ADAMTS17*, suggesting increased expression (Fig. 4D). We did not observe a distinct pattern of *ADAMTS10* or *ADAMTS17* expression based on specific skeletal elements, suggesting that both genes were expressed in autopods of the hind limb and forelimb. Lastly, the overall read counts for *ADAMTS10* and *ADAMTS17* in the stylopod and zeugopod were higher than in the autopods.

Finally, we mapped predicted binding sites of key chondrogenic and osteogenic transcription factors, including SOX9, RUNX2, and ATF4, within 5 kb upstream of the TSS using the Search Motif Tool in the Eukaryotic Promoter Database (Fig. 4F, G)[43]. Overall, transcription factor binding sites upstream of *ADAMTS10* mapped more frequently closer to the TSS (<2 kb) compared to *ADAMTS17*, with the exception of SOX9, SOX6, and ATF4 binding sites. We also noted more SOX9 binding sites upstream of the *ADAMTS17* TSS.

Collectively, these data suggest specific regions of chromatin accessibility in the vicinity of *ADAMTS10* and *ADAMTS17* and correlating with their expression in human embryonic cartilage. In addition, the mapping of chondrogenic and osteogenic transcription factor binding sites in the *ADAMTS10* and *ADAMTS17* promoter region supports the regulation of *Adamts10* and *Adamts17* expression that was observed during chondrocyte hypertrophy.

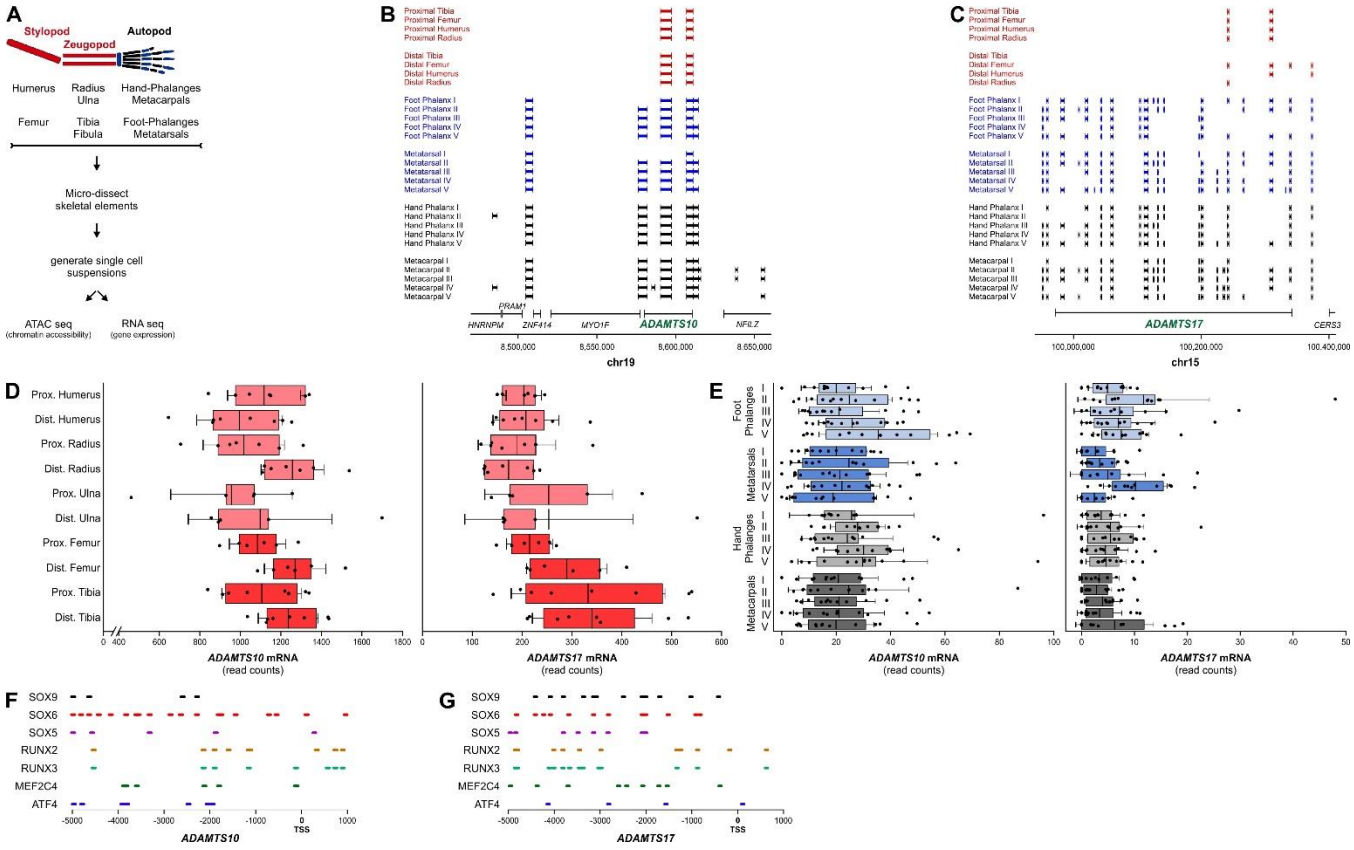

Figure 4: Chromatin accessibility and putative regulation of ADAMTS10 and ADAMTS17 in human cartilage and bone development. A) *Limb skeletal elements and experimental design to generate ATAC-seq and transcriptomics data from skeletal elements of human products from conception (E54&E67).* ***B, C)*** *Mapping of open chromatin regions identified by ATAC-seq 100 kb up- or downstream of ADAMTS10 (B) and ADAMTS17 (C). The positions of ADAMTS10 on human chromosome 19 and ADAMTS17 on human chromosome 15 are indicated.* ***D, E)*** *Normalized read counts indicating*

ADAMTS10 and ADAMTS17 mRNA abundance in skeletal elements from stylopods and zeugopods (D) and autopods (E). ***F, G)*** *Location of transcription factor binding sites 5 kb upstream of the ADAMTS10 (F) or ADAMTS17 (G) transcriptional start site (TSS).*

Adamts10 **and** ***Adamts17*** **inactivation compromised skin development and differentially regulated ECM deposition by skin fibroblasts.**

Adamts10;*Adamts17* DKO skin easily detached and ripped during shaving. We investigated this phenomenon systematically by measuring the thickness of the dermal sub-layers in Masson's trichrome stained cross-sections (Fig. 5A-E). The overall thickness of *Adamts10* KO and *Adamts17* KO dorsal skin was reduced compared to WT skin and was even further reduced in DKO skin, which was significantly thinner compared to WT and *Adamts10* KO or *Adamts17* KO skin (Fig. 5B). Epidermal layer thickness was slightly but significantly reduced in DKO skin compared to WT and *Adamts10* KO skin but not compared to *Adamts17* KO skin (Fig. 5C, left). The thickness of *Adamts10* KO and *Adamts17* KO dermis and hypodermis was significantly reduced compared to WT and further reduced in the DKO (Fig. 5C, middle, right). The panniculus carnosus (p. carnosus) muscle, which underlies mouse skin, was similarly significantly thinner in *Adamts17* KO and DKO skin sections compared to WT and *Adamts10* KO (Fig. 5D). The proportion of the hypodermis to overall skin thickness was greatly reduced in DKO skin, whereas the proportions of the dermis and p. carnosus were both increased (Fig. 5E). A similar reduction in the hypodermal layer and increase in the dermal layer were evident in *Adamts17* KO skin and to a lesser extent in *Adamts10* KO skin. We also observed a significant reduction in the number of hair follicles in DKO skin compared to all other genotypes, but no significant changes in the *Adamts10* KO or *Adamts17* KO compared to WT skin (Fig. 5F).

To identify the cellular origins of ADAMTS10 and ADAMTS17 in the skin, we data-mined the Hair-GEL database, which contains single-cell transcriptomic data from E14.5 and P5 skin with a focus on hair follicle development[44,45]. At E14.5, differential expression of *Adamts10* and *Adamts17* was noted in the dermal condensate, where *Adamts10* expression was high, and in the placode and epidermis, where *Adamts17* expression was high (Fig. 5G). In fibroblasts, Schwann cells, or melanocytes, *Adamts10* and *Adamts17* were expressed at similar levels. At P5, *Adamts10* was strongly expressed in subtypes of

dermal papilla cells and *Adamts17* was strongly expressed in the bulge stem cell population (Fig. 5H). Expression in other cell types, including fibroblasts, was much lower and differential expression of *Adamts10* and *Adamts17* was less apparent. We next validated temporal *Adamts17* expression dynamics in the skin by RNA in-situ hybridization and immunostaining of embryonic and postnatal mouse skin. At E13.5, *Adamts17* mRNA was localized predominantly in the developing epidermis (Fig. 5I). As previously described, at E16.5, high *Adamts17* mRNA levels were observed in the placode and the hair peg of the developing hair follicles, while lower *Adamts17* expression was observed in the epidermis and cells of the dermal layer (Fig. 5J)[22]. At P0, *Adamts17* mRNA was concentrated in cells surrounding the base of the hair follicle and in the outer root sheath (Fig. 5K). ADAMTS17 immunostaining in postnatal skin confirmed ADAMTS17 protein localization in or around hair follicles and the hair shaft (Fig. 5L). At later postnatal time points up to P21, *Adamts17* mRNA signal was generally low (data not shown).

Finally, we investigated fibrillin-1 and fibronectin ECM deposition in primary skin fibroblasts isolated from WT, *Adamts10* KO, *Adamts17* KO, or *Adamts10;Adamts17* DKO mice. Strikingly, skin fibroblasts from DKOs did not form a fibronectin network and showed abnormal intracellular accumulation of fibrillin-1 (Fig. 5M, N). Fibroblasts isolated from individual *Adamts10* KO or *Adamts17* KO mice showed intermediate phenotypes with a significant reduction of fibronectin in both KOs and a reduction of fibrillin-1 in the *Adamts17* KO. While fibronectin in *Adamts17* KO fibroblasts was present in globular structures or short fibers on the cell surface or in the vicinity of fibroblasts, fibronectin in *Adamts10* KO fibroblasts was largely organized in an extracellular fibrillar network. Notably, in areas of *Adamts10* KO fibroblasts ECM with sparse to no fibronectin network, intracellular fibrillin-1 accumulation was more prevalent.

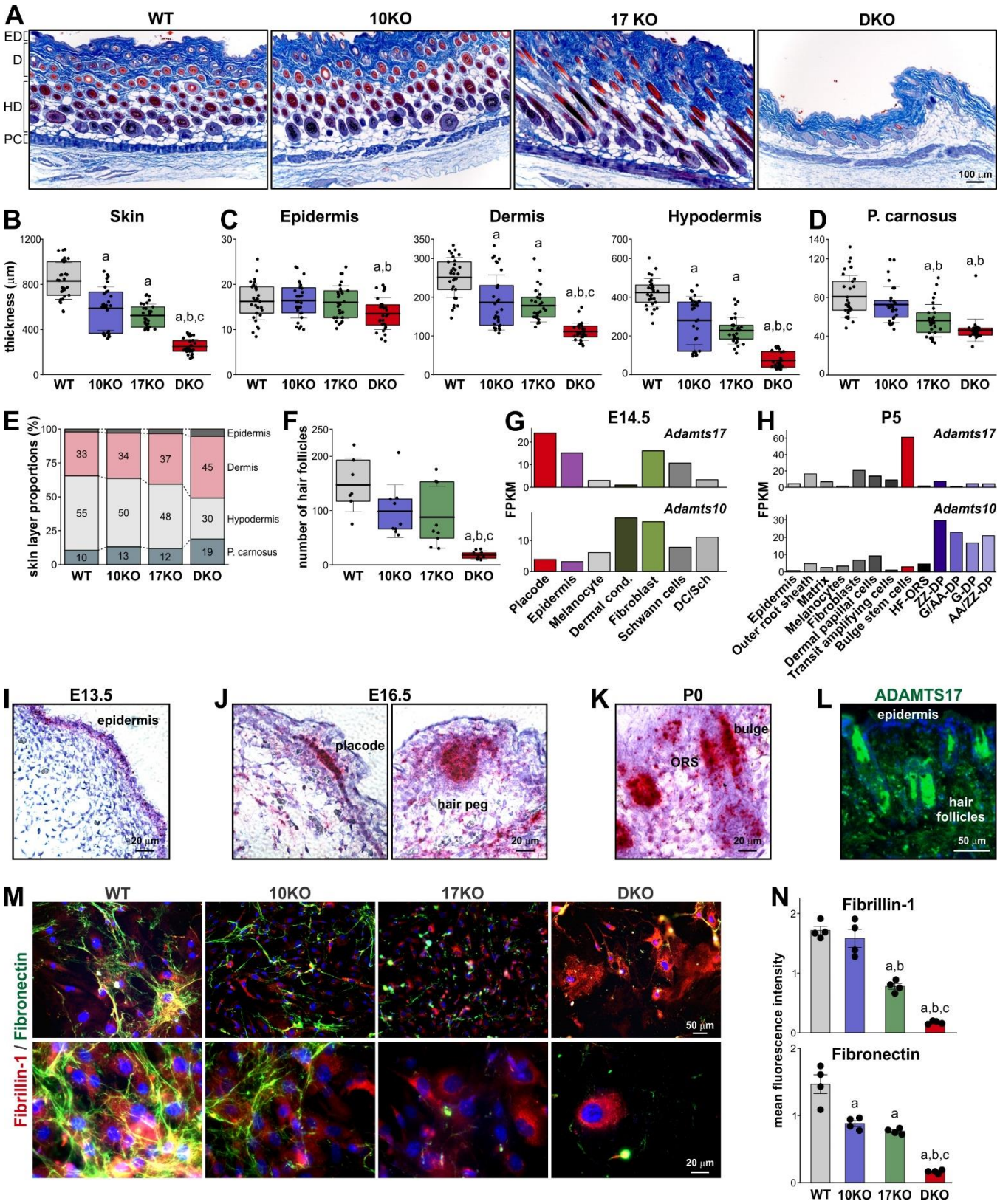

389

Figure 5. Adamts10;Adamts17 DKO is associated with skin alterations and aberrant ECM deposition by dermal fibroblasts. A) *Micrographs of Masson's trichrome-stained cross-sections through dorsal skin from 4-week-old WT, Adamts10 KO (10KO), Adamts17 KO (17KO), and DKO mice. ED, epidermis; D, dermis; HD, hypodermis; PC, panniculus carnosus.* ***B-D)*** *Bar graphs showing quantification of overall skin thickness (B) and the thicknesses of the epidermis, dermis, hypodermis (C), and panniculus carnosus (p. carnosus, D). Individual data points represent multiple measurements along the different skin layers from n=3 mice/genotype.* ***E)*** *Stacked bar graphs showing the relative proportions of individual skin layers. The percentage values are indicated.* ***F)*** *Bar graphs showing the quantification of hair follicle numbers in the skin for each genotype.* ***G, H)*** *Bar graphs showing normalized gene expression in fragments per kilobase of transcript per million mapped reads (FPKM) for Adamts10 and Adamts17 in individual skin cell types at E14.5 (G) and P5 (H). Data were extracted from the Hair-GEL database[44,45].* ***I-K)*** *Micrographs showing the localization of Adamts17 mRNA (red/dark purple) in WT skin cross-sections at E13.5 (I), E16.5 (J), and P0 (K) detected by RNAscope in-situ hybridization with a probe specific for Adamts17. Sections were counterstained with hematoxylin.* ***L)*** *Micrograph of ADAMTS17 immunostaining (green) of cross-sections through WT skin. Nuclei were stained with DAPI (blue).* ***M)*** *Micrographs of primary mouse skin fibroblasts after immunostaining for fibrillin-1 (red) and fibronectin (green). Nuclei were counterstained with DAPI (blue).* ***N)*** *Quantification of mean fluorescence intensity from M (n=4 biological replicates). In B, C, D, F, floating bars indicate 25th – 75th percentile range, lines the mean value and whiskers the standard deviation. In N, the bars represent the mean value and the whiskers the standard deviation. Statistical differences in B, C, D, F, N were determined using a one-way ANOVA with post-hoc Tukey test. a, p<0.05 compared to WT; b, p<0.05 compared to Adamts10 KO; p<0.05 compared to Adamts17 KO.*

Identification of fibronectin and COL6 as ADAMTS17 binding partners.

It was previously reported that ADAMTS10 constitutively had poor protease activity due to a degenerated furin cleavage site (GLKR instead of a canonical RX[K/R]R↓ site), which hindered furin-mediated activation (Fig. 6A)[21,31]. In contrast, ADAMTS17 is an active protease based on extensive autoproteolysis at the cell surface[22]. To identify ADAMTS17 substrates, we used an unbiased mass

spectrometry (MS)-based N-terminomics strategy, Terminal Amine Isotopic Labeling of Substrates (TAILS). We complemented this approach by yeast-2-hybrid protein-protein interaction screening. For TAILS, we co-cultured human dermal fibroblasts with HEK293 cells stably expressing ADAMTS17 or its active site mutant ADAMTS17-EA (Glu-390 to Ala), which abolishes its autocatalytic activity (Fig. 6B, left)[22]. Following isobaric tag labelling of the samples, we identified differentially abundant N-terminally labeled peptides uniquely present or elevated in ADAMTS17 conditioned medium and prioritized the peptides with neo-N-termini from secreted and/or ECM proteins as candidate substrates (Fig. 6C). Amongst potential ADAMTS17 substrates, we identified peptides from the COL1, COL6A2, and COL6A3 chains, and fibronectin (FN1). Multiple ADAMTS17 peptides were identified in the wild-type ADAMTS17 samples due to its autoctalytic activity and served as positive controls. In parallel, we used the ADAMTS17 ancillary domain (17-AD) as the bait in a yeast-2-hybrid screen to identify binding partners. This approach identified the ECM proteins thrombospondin-1 (THSB1) and fibulin-3 (FBLN3), the secreted proteases ADAM12 and PAPPA, and the extracellular domain of the catalytically inactive receptor tyrosine-protein kinase ERBB3 (Fig. 6D). Most notably, we also identified fibronectin and COL6 as potential ADAMTS17 binding partners, which overlapped with the results from the MS screen. Therefore, we selected fibronectin and COL6 for further investigation and validation as potential ADAMTS17 substrates.

Based on the yeast-2-hybrid data, the ADAMTS17 ancillary domain interacted with the C-terminal region of fibronectin comprising FNIII domain #15 and FNI domains #10-12 (amino acid residues 2130 – 2416, NP_997647) (Fig. 6E, F). The N-terminally labeled fibronectin peptide identified in the MS approach localized to the same region (amino acid residues 2282 – 2317) and covered the linker region between FNIII #15 and FNI #10 and the N-terminal part of FNI #10. For biochemical validation of fibronectin as an ADAMTS17 substrate, we first used western blot of conditioned medium and cell lysates collected from human dermal fibroblasts co-cultured with ADAMTS17- or ADAMTS17-EA-expressing HEK293 cells equivalent to the MS approach (Fig. 6B, left). Using five different antibodies against fibronectin, we detected distinct fibronectin fragmentation patterns in conditioned medium in the presence of ADAMTS17-, but not ADAMTS17-EA-expressing HEK293s (Fig. 6G). All antibodies were raised against full length plasma fibronectin, except 15613-1-AP (ProteinTech), which was raised against a region comprising FNIII domain #15 and FNI domains #10-12. Fibronectin fragmentation in

the cell lysate, which included the ECM fraction, was not observed. Together, this suggested that ADAMTS17 protease activity correlated with fibronectin fragmentation. To more directly test if ADAMTS17 can cleave fibronectin, we co-transfected HEK293 cells with ADAMTS17 or ADAMTS17-EA-encoding plasmids and a plasmid encoding V5-tagged fibronectin (rFN) (Fig. 6B, right). When we analyzed conditioned medium and cell lysates harvested after co-expression of these plasmids, we did not detect fibronectin fragmentation in the medium or cell lysate with a polyclonal antibody against fibronectin or an antibody against the V5 tag of rFN (Fig. 6H). This suggested that fibronectin may not be a direct ADAMTS17 substrate, or that ADAMTS17 selectively cleaved fibronectin fibrils, which are assembled by dermal fibroblasts.

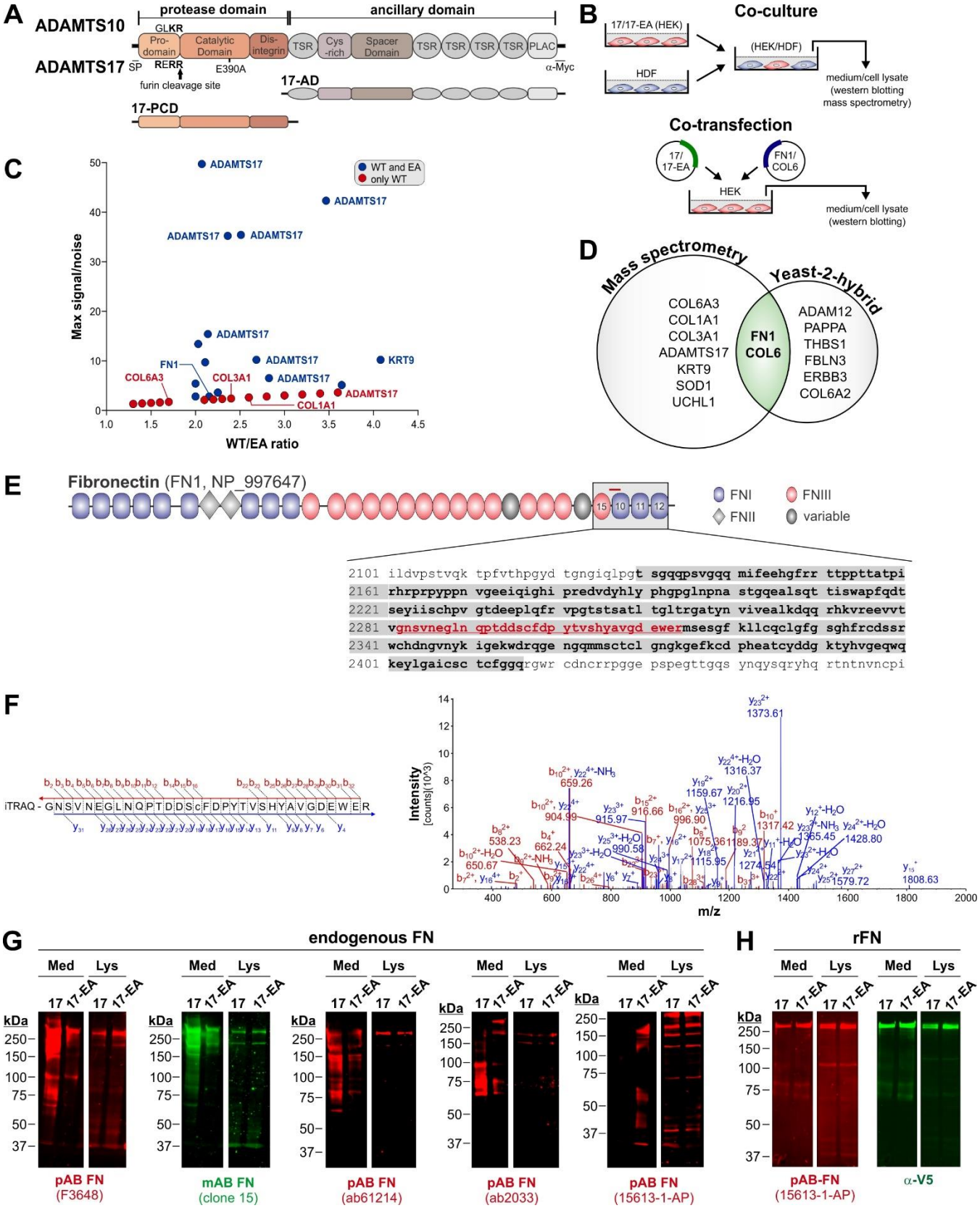

Figure 6. Identification of fibronectin as a potential ADAMTS17 substrate. A) *Domain organization of ADAMTS10 and ADAMTS17, which are identical. The degenerate (ADAMTS10) and canonical (ADAMTS17) furin processing sites and the localization of the catalytic residue Glu-390 in ADAMTS17 (17) that was mutated into Ala to generate proteolytically inactive ADAMTS17-EA (17-EA) are indicated. The domain organization of the catalytic (17-PCD) and ancillary (17-AD) domain constructs is indicated.* ***B)*** *Schematic representation of experimental design for co-culture of human dermal fibroblasts (HDF) with HEK293 cells stably expressing 17- or 17-EA (left) or co-transfection of 17- or 17-EA-encoding plasmids with FN1 or COL6A2-encoding plasmids in HEK293 cells (right).* ***C)*** *Volcano plot showing N-terminally labeled peptides identified by N-terminomics method TAILS in conditioned medium from ADAMTS17-expressing HEK293 cells co-cultured with HDFs. Peptides present only in samples from WT ADAMTS17 (red) or enriched in conditioned medium from WT ADAMTS17 co-cultures compared to the co-cultures with proteolytically inactive ADAMTS17-EA suggest ADAMTS17 substrates.* ***D)*** *Venn diagram showing overlap of ADAMTS17-cleaved proteins (TAILS) from co-culture systems (left) and binding partners for the ADAMTS17 ancillary domain (17-AD) identified by yeast-2-hybrid screening with a human placenta-derived cDNA library (right). Note that fibronectin (FN1) and COL6 were independently identified in both screens.* ***E)*** *Domain organization of fibronectin (FN1, NP_997647) showing the localization of the domains that interacted with 17-AD (grey box, bolded amino acid sequence) and the localization of the peptide identified by TAILS (red bar, red amino acid sequence).* ***F)*** *MS2 spectrum of the N-terminally labeled FN1 peptide (GNSVNEGLNQPTDDSCFDPYTVSHYAVGDEWER) showing b and y ions.* ***G)*** *Western blot detection of endogenous fibronectin in conditioned medium (Med) and cell lysates (Lys) collected after co-culture of 17 or 17-EA-expressing HEKs with HDFs. A monoclonal (green) and four different polyclonal (red) anti-fibronectin antibodies were used.* ***F)*** *Western blot detection of recombinant fibronectin (rFN) in conditioned medium (Med) and cell lysate (Lys) collected after co-expression of 17 or 17-EA with rFN in HEK293 cells. A polyclonal anti-fibronectin antibody (red) and a monoclonal anti V5-tag antibody (green) were used to detect rFN.*

For COL6A2, the yeast-2-hydrid data suggested an interaction region for 17-AD comprising the C-terminal portion of the central triple helical domain and an N-terminal portion of the von Willebrand factor A (VWA) domain #C1 (amino acid residues 480 – 652, NP_001840.3) (Fig. 7A). TAILS identified an

N-terminally labeled peptide originating from COL6A3 (amino acid residues 1348 – 1367, NP_004360.2), which was localized in the C-terminal portion of VWA domain #N4 (Fig. 7B, C). For validation of COL6 as ADAMTS17 substrate, we used the cell culture setups shown in Fig. 6B. In the co-culture system of ADAMTS17-expressing HEKs with HDFs, we did not observe a different pattern of bands originating from endogenous COL6 in conditioned medium in the presence of active ADAMTS17 as detected with a COL6 antibody (Fig. 7D). However, we noticed the disappearance of a ~125 kDa COL6-reactive band in the cell lysate/ECM fraction when proteolytically active ADAMTS17 was present. When visualizing COL6 ECM deposition in this co-culture system by immunostaining, we observed reduced COL6 staining in the presence of ADAMTS17 compared to ADAMTS17-EA (Fig. 7E, F). We observed a similar difference when fibroblasts were cultured in the presence of cell-free conditioned medium collected from ADAMTS17- or ADAMTS17-EA-expressing HEK293 cells. In the presence of ADAMTS17, COL6 in the ECM was lower than the amount of COL6 deposited in the presence of ADAMTS17-EA (Fig. 7G, H). These observations would be consistent with proteolytically active ADAMTS17 limiting the amount of COL6 deposited in the ECM, potentially via proteolysis, but could also be explained by inactive ADAMTS17-EA promoting COL6 deposition into the ECM. To determine, if COL6 is a direct ADAMTS17 substrate, we co-expressed FLAG-tagged recombinant (r)COL6A2 with ADAMTS17 or ADAMTS17-EA in HEK293 cells. Using western blot detection of the FLAG-tag, we did not observe rCOL6A2 fragmentation in the medium or cell lysate and only detected full length COL6A2 (Fig. 7I). However, we noticed an increase in the band intensity for COL6 in the ADAMTS17-EA lysate, which could be the result of decreased proteolysis or increased cellular retention or cell surface/ECM association. To determine, if ADAMTS17 co-localized with COL6, we cultured fibroblasts producing endogenous COL6, in the presence of the previously described purified recombinant catalytic ADAMTS17 domains (17-PCD) or its ancillary domains (17-AD) and co-immunostained for endogenous COL6 and recombinant ADAMTS17 (α-Myc)[22]. Endogenous COL6 in the ECM of fibroblasts costained with both ADAMTS17 protein constructs, suggesting the possibility of an interaction in the ECM that could be the basis for selective proteolysis of COL6A3 (Fig. 7J). Finally, we analyzed endogenous COL6 distribution and ECM deposition in dermal fibroblasts isolated from a patient with WMS due to a ADAMTS17 Thr343Ala mutation, where we previously showed intracellular retention and reduced ECM deposition of fibronectin, fibrillin-1, and COL1[10]. Compared to control adult human dermal fibroblasts,

we observed a strong reduction of COL6 ECM deposition in WMS dermal fibroblasts and concurrent intracellular COL6 accumulation (Fig. 7K, L). This observation was confirmed by western blot analysis, where COL6 was decreased in the medium from WMS patient-derived dermal fibroblasts and increased in the cell lysate compared to adult human dermal fibroblasts (Fig. 7M, N). Collectively, our data suggest that fibronectin and COL6 are potential ADAMTS17 binding partners and/or substrates.

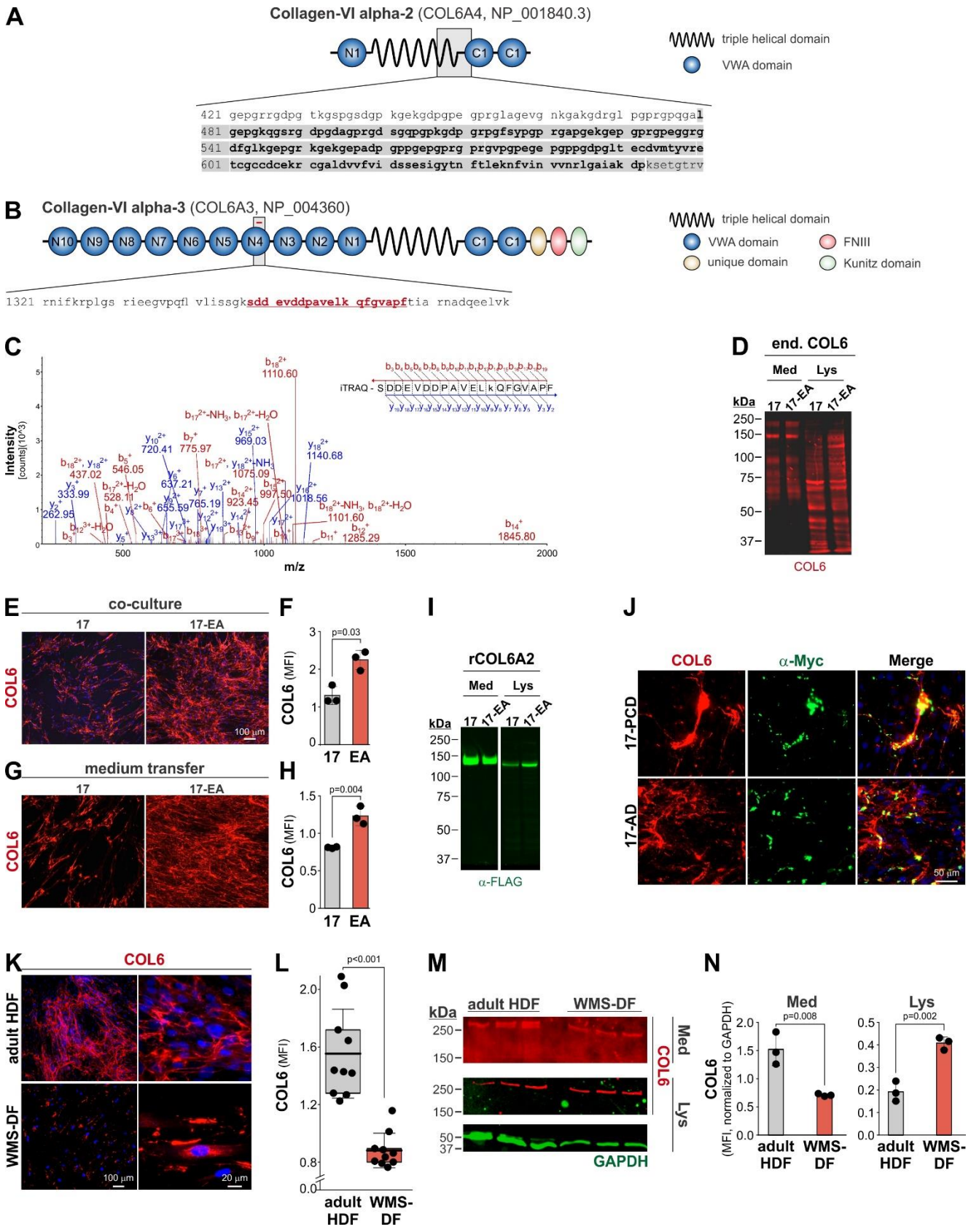

522

Figure 7. Identification of collagen VI (COL6) as an ADAMTS17 interacting protein and potential substrate. A) *Domain organization of COL6A2 (NP_0018403) showing the localization of the domains that interacted with 17-AD (grey box, bolded amino acid sequence.* ***B)*** *Domain organization of COL6A3 (NP_004360) showing the localization of the peptide identified by MS (red bar, red amino acid sequence).* ***C)*** *MS2 spectrum of the N-terminally labeled ADAMTS17-digested COL6A3 peptide (SDDEVDDPAVELkQFGVAPF) showing b- and y-ions.* ***D)*** *Western blot of endogenous (end.) COL6 (red) in conditioned medium (Med) and cell lysate (Lys) collected from co-cultures of 17 or 17-EA-expressing HEK293 cells with HDFs.* ***E)*** *Micrographs of endogenous COL6 deposition (red) in the ECM of HDFs co-cultured with 17- or 17-EA-expressing HEK293 cells. Nuclei were stained with DAPI (blue).* ***F)*** *Quantification of the mean fluorescence intensity of the COL6 signal (n=3 replicates).* ***G)*** *Micrographs of endogenous COL6 deposition (red) in the ECM of HDF after culture in the presence of conditioned medium from 17- or 17-EA-expressing HEK293 cells. Nuclei were stained with DAPI (blue).* ***H)*** *Quantification of the mean fluorescence intensity of the COL6 signal (n=3 replicates).* ***I)*** *Western blot of recombinant COL6 (rCOL6) in conditioned medium (Med) and cell lysate (Lys) collected after co-expression of 17 or 17-EA and rCOL6A2 in HEK293 cells using a monoclonal anti FLAG-tag antibody (green).* ***J)*** *Micrographs of HDFs cultured in the presence of 50 μg/ml of purified recombinant 17-PCD and 17-AD protein (see Fig. 5A for domain organization) co-stained for endogenous COL6 (red) and the Myc-tag of the recombinant ADAMTS17 protein fragments (green). Nuclei were stained with DAPI (blue).* ***K)*** *Micrographs of adult HDFs and WMS-patient-derived dermal fibroblasts (WMS-DF) for endogenous COL6 (red). Nuclei were counterstained with DAPI (blue).* ***L)*** *Quantification of the mean fluorescence intensity of the COL6 signal (n=3 replicates, 2-3 fields-of-view).* ***M)*** *Western blot of endogenous COL6 (red) and GAPDH (green) in conditioned medium (Med) and cell lysate (Lys) collected from HDF and WMS-DF cultures.* ***N)*** *Quantification of COL6 band mean fluorescence intensities normalized to GAPDH. In E, G, M, bars represent the mean value and whiskers the standard deviation. In K, the floating bars indicate the 25^{th} – 75^{th} percentile range, the lines the mean value and whiskers the standard deviation. Statistical differences in E, G, K, M were determined using a two-sided Student t-test.*

Discussion

The fact that mutations in *ADAMTS10* and *ADAMTS17* can both cause short stature in WMS unequivocally implicates both genes in the regulation of bone growth via an impact on growth plate function. Since it is unclear if and how both genes interact or cooperate in this process, we analyzed the phenotypes of *Adamts10*;*Adamts17* DKO mice. We showed that combined inactivation of ADAMTS10 and ADAMTS17 exacerbated bone shortening when compared to individual KOs with ADAMTS17 gene dosage having an apparently stronger effect and compromised postnatal survival. In addition, we showed that ADAMTS10 and ADAMTS17 are required for skin development, which may relate to stiff and thickened skin described in WMS patients[3,46]. Finally, we identified fibronectin and COL6 as potential ADAMTS17 substrates in high-throughput unbiased screens. This could point towards a potentially distinct function for ADAMTS17 as a regulator of ECM formation and homeostasis. Indeed, such a function is known for ADAMTS10, specifically in the enhancement of fibrillin-1 assembly, since endogenous ADAMTS10 is only slightly activated by furin[21].

Bone growth is largely driven by chondrocyte proliferation in the growth plate and their subsequent hypertrophic expansion. The disruption of either process can result in bone shortening and short stature[37,47-49]. The reduction in the width of the hypertrophic zone observed in the DKO growth plate could thus be attributed to decreased formation and/or accelerated turnover of hypertrophic chondrocytes, which depend on chondrocyte proliferation and matrix metalloprotease (MMP)-mediated ECM remodeling at the ossification front, respectively[50-52]. Since we did not observe changes in the dimensions of the proliferative zone, we suggest that hypertrophic *Adamts10*;*Adamts17* DKO chondrocytes turnover faster. Hypertrophic chondrocyte turnover requires the transition of a cartilage ECM towards a bone ECM that is primed for mineralization. Key enzymes that regulate these processes include MMP13 and MMP9, which can cleave COL2 and COL10 or promote the vascularization of the growth plate[51,52]. When MMP13 or MMP9 were inactivated, the length of the hypertrophic zone in developing bones was increased by ~70% and primary ossification was delayed, indicating a delay in chondrocyte turnover, in particular chondrocyte apoptosis[51,52]. Since we observed a shorter hypertrophic zone, we postulate that ADAMTS10 and ADAMTS17 may attenuate chondrocyte turnover

potentially by regulating the activity of MMP13 or MMP9[53]. In this context, it is interesting to note that ADAMTS10 WMS knock-in and ADAMTS17 KO mice show opposite growth plate phenotypes, each resulting in reduced bone length. The knock-in of the ADAMTS10 Ser236X mutation (Arg237X in humans) resulted in an expansion of the hypertrophic zone, which correlated with a 6-10% reduction in long bone length[34]. In contrast, inactivation of *Adamts17* resulted in a shorter hypertrophic zone, which also correlated with a 6-10% reduction long bone length[33]. In *Adamts17* KO mice, however, chondrocyte proliferation or apoptosis was not changed[33]. These reports would suggest that ADAMTS10 and ADAMTS17 have distinct roles in regulating growth plate activity and chondrocyte hypertrophy, both resulting in shorter bones. This interpretation is further supported by our findings reported here, that maturation and mineral deposition in ADAMTS17-deficient primary chondrocytes was strongly reduced, but unaffected in ADAMTS10-deficient chondrocytes. The latter findings could also be explained by differential compensation, where ADAMTS17 can compensate for the lack of ADAMTS10 in primary chondrocytes, but not vice versa. As an alternative explanation, ADAMTS10 and ADAMTS17 could regulate signaling pathways that drive growth plate activity and bone growth. In this context, it was shown that reduced BMP signaling in *Adamts17* KO mice delayed terminal differentiation of chondrocytes[33]. In the skin of *Adamts10* WMS knock-in mice, BMP signaling but not TGFβ signaling was similarly reduced[34]. How ADAMTS10- or ADAMTS17-deficiency translates into reduced BMP signaling is not clear, but could be secondary to changes in fibronectin and fibrillin-1 deposition, which regulates extracellular BMP activity[54,55]. Taken together, our data and data from others are consistent with ADAMTS10 and ADAMTS17 regulating different aspects of growth plate activity with ADAMTS17 having a stronger effect.

Skin thickening is a feature of WMS syndrome, and decreased skin elasticity in *Adamts10* KO and *Adamts17* KO mice as well as increased skin thickness in *Adamts10* WMS knock-in mice were reported previously[31,33,34]. In contrast, we noticed fragile skin during routine handling of *Adamts10*;*Adamts17* DKO mice and, accordingly, observed reduced skin thickness in *Adamts10*;*Adamts17* DKO mice, which was predominantly driven by a reduction in the hypodermal layer. This suggested that ADAMTS10 and ADAMTS17 play a role in skin development or postnatal homeostasis, with likely partial compensation in the individual KOs given the much stronger phenotype observed for the *Adamts10*;*Adamts17* DKO skin. One reason for these contrasting observations could be that skin thickening was previously

609 observed in older mice, i.e. at 3 and 8 months of age in the *Adamts17* KO and at 3 months of age in the
610 *Adamts10* WMS knock-in[33,34]. Therefore, it is possible that the skin thickness might increase in our
611 individual KOs with age. We previously demonstrated that WMS patient-derived dermal fibroblasts
612 harboring an *ADAMTS17* mutation were deficient in secretion and deposition of ECM proteins, in
613 particular fibronectin, fibrillin-1 and COL1[10]. When we examined ECM deposition in primary DKO
614 mouse skin fibroblasts, we also observed compromised ECM deposition. In the absence of both
615 ADAMTS10 and ADAMTS17, fibronectin deposition was almost completely abolished and fibrillin-1
616 appeared to be retained intracellularly. Individual KOs displayed intermediate phenotypes with a more
617 profound phenotype in *Adamts17*KO fibroblasts and a somewhat milder phenotype in *Adamts10*KO
618 fibroblasts. In *Adamts17*KO fibroblasts, fibronectin was deposited as globular speckles, but did not
619 form elongated fiber-like structures or ECM networks. In *Adamts10*KO fibroblasts, fibronectin did form
620 fibers and ECM networks, but they were less dense compared to WT fibroblasts and showed regions
621 void of fibronectin networks. Interestingly, in these regions intracellular fibrillin-1 immuno-reactivity
622 was more apparent. Collectively, these data support a model where ADAMTS17 regulates the secretion
623 and/or assembly of fibronectin by remodeling fibronectin fibrils, which are required for the formation
624 of stable fibrillin-1 networks, whereas ADAMTS10 plays a more “downstream” role where it could
625 enhance fibrillin-1 assembly as suggested previously[21,41,56].

626 Since ADAMTS10 and ADAMTS17 are members of the ADAMTS protease family they are presumed to
627 fulfil their biological function through their respective protease activities. However, ADAMTS10 is the
628 only ADAMTS protease with a degenerated furin cleavage site (GLKR↓, lacking a canonical Arg residue
629 at the P4 position) and is incompletely activated by furin-mediated removal of the inhibitory
630 prodomain[21]. It was shown that ADAMTS10 could cleave fibrillin-1 and fibrillin-2 efficiently after
631 restoring a canonical furin recognition site (RRKR↓) by mutagenesis, suggesting that ADAMTS10 has
632 intrinsic protease activity when activated[21,31]. In *Adamts10* KO and *Adamts10* WMS knock-in mice,
633 fibrillin-2 accumulation in the ciliary zonule of the eye was observed and could be explained by the
634 absence of “fibrillin-ase” activity in ADAMTS10-deficient tissue. Indeed, furin activated ADAMTS10
635 cleaves fibrillin-2[31]. However, fibrillin-2 accumulation could also be explained by ADAMTS10 promoting
636 the assembly of fibrillin-1, which would be reduced in the *Adamts10* KO and result in increased fibrillin-
637 2 exposure to antibodies in the fibrillin microfibril bundles of the ciliary zonule[21,31,34]. Alternatively,

638 ADAMTS10 could be involved in promoting the switch from developmental fibrillin-2-rich microfibrils
639 to postnatal fibrillin-1-rich microfibrils, which similarly would be lacking or be reduced in ADAMTS10-
640 deficient tissues. Therefore, it is plausible that ADAMTS10 may primarily regulate ECM formation both
641 via protease-dependent and protease-independent activities on fibrillin-2 and fibrilin-1 respectively,
642 modulating the formation and isoform composition of fibrillin microfibrils. For ADAMTS17, we showed
643 that it cleaves itself at multiple sites, including in the active site, and is thus proteolytically active[22].
644 Therefore, we used a complementary MS and yeast-2-hybrid approach in the quest to uncover
645 ADAMTS17 substrates. In both screens, fibronectin and COL6 were identified as potential substrates
646 and binding partners for ADAMTS17.

647 In summary, this study provides evidence that ADAMTS10 and ADAMTS17 may operate in distinct ways
648 in the pathways that regulate bone growth and skin development through regulation of ECM
649 deposition and turnover and provide additional understanding of the mechanisms underlying WMS.

650

651 **Materials and Methods**

652 **Mouse models**

653 *Adamts10* KO mice generated by Deltagen Inc. and their genotyping were described previously[31]. In
654 brief, 41 bp of *Adamts10* exon 5 were replaced with an IRES-lacZ-neo cassette resulting in a frameshift
655 and a premature stop codon triggering nonsense-mediated mRNA decay of the *Adamts10* mRNA. The
656 mice were licensed from Deltagen Inc. (agreement #AGR-17486) and maintained in the C57BL/6 strain.
657 *Adamts17* KO mice were generated in C57BL/6 ES cells by CRISPR/Cas9-induced non-homologous end-
658 joining mutagenesis by contract to Applied StemCell, Inc. A guide RNA targeting *Adamts17* exon 3 (5'-
659 GTCCCTCCACCTCCGTAGCA-3') was co-injected with Cas9 protein into blastocysts to generate F0 mice,
660 which were screened for frameshift-causing indels. F0 mice harboring an AT insertion in *Adamts17*
661 exon 3 were identified by Sanger sequencing and used to generate F1 mice with the germline-
662 transmitted *Adamts17* AT insertion. F1 mice harboring the AT insertion were identified by Sanger
663 sequencing of a PCR product generated with primers adjacent to exon 3 (F primer: 5'-
664 GAGAGCATCTGATCAGACGCAAATGG-3', R primer: 5'-CATGTGACCCACAGAGTGTCAGC-3'). *Adamts17* KO
665 mice were rederived at the Icahn School of Medicine. *Adamts17* Het and KO mice were genotyped

using DNA from clipped toes as template for a PCR reaction with the following primers: TS17-F 5'-CAGCAGACAGAAGCACAAGCC-3' and TS17-R 5'-TAGAATCATGGCCCTGACACC-3'. The resulting PCR product was isolated and submitted for Sanger sequencing using the TS17-F primer (Psomagen). The *Adamts17* mutant was maintained in the C57BL/6 strain. Mice heterozygous for the *Adamts10* KO and *Adamts17* KO alleles were crossbred to generate *Adamts10* Het;*Adamts17* Het mice, which were then crossbred to generate *Adamts10*;*Adamts17* DKO mice. *Adamts10* Het or *Adamts17* Het mice were crossbred to generate age- and sex-matched WT, *Adamts10* KO, or *Adamts17* KO mice. Mice were used between 4-8 weeks of age and data from both sexes were combined. All mouse experiments were approved by the Institutional Animal Care and Use Committee (IACUC) of the Icahn School of Medicine at Mount Sinai (protocol numbers IACUC-2018-0009, PROTO202000259, and TR202300000105).

X-ray imaging

After sacrifice, intact mouse limbs were imaged using a high-resolution radiographic system (UltraFocus digital X-ray cabinet, Faxitron Bioptics). A 10 mm metal rod was used as a scale to enable quantification of bone length.

Histology

Limbs from 4-week-old mice were disarticulated and the tibia and femur cut mid-shaft to dissect the knee joint. Muscle and other soft tissue were removed and the knee was fixed in Z-fix (Electron Microscopy Science) for 48 h. After decalcification in 14% EDTA solution, the knee joints were dehydrated, embedded in paraffin and sectioned through the middle of the knee. Sections were then stained with hematoxylin & eosin (H&E) for histomorphometry. Proximal tibial growth plates were imaged and the dimensions of the growth plate regions measured at multiple points across the growth plate using ImageJ Fiji (NIH)[57,58]. Dorsal skin was first shaved to remove hair, and a full thickness rectangular strip was dissected and flattened on filter paper. The filter paper with the skin was then immersed in Z-Fix Zinc Formalin Fixative for 24h, processed and paraffin embedded. Cross sections

were stained with Masson's trichrome stain and imaged. Skin thickness and the thickness of individual skin layers was measured from micrographs using ImageJ Fiji.

Cell culture assays

Human embryonic kidney (HEK) 293 cells (CRL-1573) and adult human dermal fibroblasts (HDF, PCS-201-012) were purchased from ATCC. Isolation and characterization of the WMS patient-derived dermal fibroblasts (WMS-DF) harboring the *ADAMTS17* c.1027A>G (p.Thr343Ala) mutation was described previously[10]. Cells were cultured in Dulbecco's Modified Eagle Medium (DMEM) supplemented with 10% fetal bovine serum (FBS), 1% L-glutamine, 100 units/ml penicillin and 100 mg/ml streptomycin (PSG) (complete DMEM) in a 5% CO_2 atmosphere in a humidified incubator at 37 °C. Upon reaching confluence, cells were split in a 1:10 (HEK293) or 1:3 (fibroblasts) ratio. Primary fibroblasts were used up to passage 5-7. HEK293 cells stably expressing ADAMTS17 or ADAMTS17-EA were described previously and maintained in complete DMEM supplemented with geneticin (G418)[22]. For co-culture assays, HDFs and 2×10^6 ADAMTS17 or ADAMTS17-EA (4×10^6 cells total) were combined and seeded on a 10 cm cell culture dish. After reaching confluency the cell layer was rinsed with PBS and cultured in serum free DMEM. After 48 h, conditioned medium was collected and proteins were precipitated with 10% trichloroacetic acid. The cell layer was lysed in RIPA buffer (0.1% NP40, 0.05% DOC, 0.01% SDS in PBS). Equal volumes were mixed with 5x reducing SDS loading buffer, boiled at 100 °C and separated via SDS-PAGE for western blotting. For direct ADAMTS17 proteolysis assays, HEK293 cells were co-transfected with ADAMTS17 or ADAMTS17-EA and plasmids encoding FN1 or COL6A2 using Lipofectamine 3000. The plasmid encoding V5-tagged fibronectin was described recently and kindly provided by Dr. Dieter Reinhardt (McGill University, Montreal, Canada)[59]. The COL6A2-encoding plasmid was purchased from Genscript (OHu18654D). After 24 h, cell layers were rinsed with PBS and cultured in serum-free DMEM for an additional 48 h. Conditioned medium was collected and cleared from cell debris by centrifugation. The cell layer was lysed in RIPA buffer, transferred into an Eppendorf tube and cleared of debris by centrifugation. Equal volumes were combined with 5x reducing SDS loading buffer, boiled at 100 °C and separated via SDS-PAGE for western blotting.

720

721 **Western blotting**

722 The proteins in equal volumes of media or cell lysates were separated on polyacrylamide gels using
723 SDS-PAGE and blotted onto polyvinylidene difluoride (PVDF) membranes (Immobilon-FL, Merck
724 Millipore Ltd.) using the semi-dry Bio-Rad trans-Blot® Turbo transfer system for 33 min at 25 V (Bio-
725 Rad) or a wet transfer system for 1.5 h at 70 V at 4 °C both operated with 25 mM Tris, 192 mM glycine,
726 20% methanol as transfer buffer. Membranes were blocked with 5% (w/v) milk in TBS (10 mM Tris-HCl,
727 pH 7.2, 150mM NaCl) for 1 h at RT and incubated with the following primary antibodies diluted in 5%
728 (w/v) milk in TBS-T (TBS + 0.1% Tween 20) at 4 °C overnight: polyclonal antibodies against fibronectin
729 (F3648, 1:1,000, Sigma; ab2033, 1:200, Millipore; 15613-1-AP, 1:1000, ProteinTech; ab61214, 1:200,
730 Abcam), monoclonal antibody against fibronectin (cl 15, 1:400, Sigma), polyclonal antibody against
731 COL6 (ab6588, 1:500, Abcam), monoclonal antibodies against the V5-tag (mAB, 1:500, Invitrogen) and
732 the FLAG-Tag (M2, 1:500, Sigma), or a monoclonal antibody against GAPDH (1:1,000, Millipore). After
733 incubation with the primary antibody, membranes were rinsed with TBS-T 3 × 5 min at RT and
734 incubated with IRDye-goat-anti-mouse or goat-anti-rabbit secondary antibodies (1:10,000 in 5% (w/v,
735 Jackson ImmunoResearch Laboratories) in TBS-T for 2 h at RT. Membranes were then rinsed 3 × 5 min
736 with TBS-T, once in TBS and imaged using an Azure c600 Western blot imaging system (Azure
737 Biosystems). Band intensities were quantified using the AzureSpot analysis software and normalized to
738 GAPDH.

739

740 **Immunostaining of tissue sections and cell layers**

741 Growth plate and skin sections were de-paraffinized and rehydrated followed by protease-mediated
742 antigen retrieval using HistoZyme (Diagnostic BioSystems). After blocking with 5% BSA in PBS, sections
743 were incubated with a mouse monoclonal antibody against ADAMTS17, which was raised against
744 human ADAMTS17 (3B7, 1:500, Novus Biologicals) in blocking buffer in a humidified chamber overnight
745 at 4 °C. Sections were rinsed in PBS 3 × 10 min at RT and incubated in AlexaFluor 488-labeled
746 secondary goat-anti-mouse antibody in blocking buffer at for 1 h at RT. Slides were cover-slipped with

ProLong Antifade Gold mounting medium and imaged using a Zeiss Axio Observer Z1 Fluorescence Motorized Microscope w/Definite Focus.

HEK293 cells and HDFs or co-cultures thereof, or primary chondrocytes were seeded in 8-well chamber slides (50,000 cells/well) (Celltreat Scientific Products) and cultured in complete DMEM for 3-4 days. For the analysis of COL6, complete DMEM was supplemented with 100 μM ascorbic acid (ThermoFisher). After medium removal, cell layers were rinsed with PBS and fixed for 5 min with 150 μl ice-cold 70% methanol/30% acetone (Thermo-Fisher), which permeabilized the cells, or with 4% PFA for 20 min to only stain cell surface and ECM proteins, followed by permeabilization with 0.1% Triton X-100 prior to incubation with the secondary antibody. After fixation, cells were rinsed with PBS and blocked with 10% normal goat serum (Jackson ImmunoResearch Laboratories) in PBS for 1 h at RT. For Okadaic acid (Sigma Aldrich #459620) chondrocytes were treated with 50nM Okadaic acid and the controls were treated with DMSO for 24 hours and allowed to differentiate. For immunostaining cells were fixed with 4% PFA without permeabilization. Cells were incubated with primary antibodies against fibrillin-1, fibronectin, COL6, anti-Myc-tag, or ADAMTS17 diluted in blocking buffer overnight at 4 °C. Cells were rinsed 3 × 5 min with PBS and incubated with AlexaFluor labeled secondary goat-anti-mouse or goat-anti-rabbit antibodies (1:350 in blocking buffer) (Jackson ImmunoResearch Laboratories) for 2 h at RT followed by 3 × 5 min rinses with PBS and mounting with ProLong Gold Antifade Reagent with DAPI (Thermo-Fisher). Slides were imaged using a Zeiss Axio Observer Z1 Fluorescence Motorized Microscope w/Definite Focus and Zeiss Zen Microscope Software and ImageJ Fiji were used to quantify fluorescence pixel intensities.

10T1/2 pellet culture for chondrocyte-like differentiation

C3H/10T1/2 cells (CCL-226) were purchased from ATCC and cultured according to ATCC's instructions in Eagle's Basal medium[60,61]. For maintenance, cells were sub-cultured prior to confluence. For pellet cultures, C3H/10T1/2 cells were detached with trypsin-EDTA and 5×10^5 cells/ml were centrifuged at 500 g for 5 min in 15-ml tubes and cultured in serum-free DMEM supplemented with 0.1 μM dexamethasone, 0.2 mM L-ascorbic acid-2 phosphate, insulin-transferrin-selenium supplement and 10 ng/ml TGF-β1. The medium was changed every 48 h.

775

776 **mRNA isolation and quantitative real-time PCR**

777 Chondrocyte pellets were removed at the experimental time points, immersed in TRIzol reagent and
778 RNA was extracted according to the manufacturer's instructions. Pellets were lysed by pipetting the
779 TRIzol up and own several times to ensure complete homogenization. The lysate was collected into
780 sterile tubes and incubated at room temperature for 5 min. Following lysis, 0.2 ml chloroform was
781 added per 1 ml of TRIzol, the Eppendorf tubes were inverted several times and incubated at RT for 2-3
782 minutes. To separate the organic and inorganic phase, samples were centrifuged at 12,000 g for 15 min
783 at 4 °C. The aqueous phase containing RNA was carefully transferred to a new Eppendorf tube and the
784 RNA was precipitated by adding 0.5 ml of isopropanol per 1 ml of TRIzol reagent and samples were
785 incubated for 10 min at RT. The RNA was pelleted by centrifugation at 12,000 g for 10 min at 4 °C. The
786 supernatant was discarded and the RNA pellet was washed with 1 ml 75% ethanol per 1 ml of TRIzol,
787 followed by centrifugation at 7,500 g for 5 min at 4 °C. The RNA pellet was air-dried for 5-10 min at RT
788 and dissolved in 30 – 50 μl of RNase-free water depending on pellet size. RNA concentration and purity
789 were measured using a Nanodrop OneC spectrophotometer (ThermoFisher). RNA preparations were
790 further purified using DNAse I to remove traces of DNA. Reverse transcriptase was used to convert 1 μg of
791 RNA into cDNA.

792 Quantitative real-time (qRT)-PCR was performed in triplicates in a 384-well plate format. For each
793 reaction, 2 μl cDNA, 0.5 μl of forward and reverse primers (100 μM stock) and SYBR Green PCR Master
794 Mix (Applied Biosystems) were combined in a total reaction volume of 10 μl. The amplification and
795 detection were performed on an ABI PRISM 7900HT Sequence Detection System (Applied Biosystems).
796 All reactions were run under standard cycling conditions. The following PCR primer pairs were used:
797 *Gapdh* (F: 5'-AGGTCGGTGTGAACGGATTTG-3', R: 5'GGGGTCGTTGATGGCAACA-3' or F: 5'-
798 CTTTGTCAAGCTCATTTCCTGG-3', R: 5'-TCTTGCTCAGTGTCCTTGC-3'), *Adamts10* (F: 5'-
799 CCCGCCTATTCTACAAGGTGG-3', R: 5'- GCCTTCCCGTGTCCAGTATTC-3' or F: 5'-
800 GTAGTGGAGTGCCGAAATCAG-3', R: 5'-CAGCGTGACCAGTTTCCTAC-3'), *Adamts17* (F: 5'-
801 CTGCTGTATTTGTGACCAGGAC-3', R: 5'- AGCACACATTTCCTCTTAGCAC-3' or F: 5'-
802 CCTTTACCATCGCACATGAAC-3', R: 5'-ATTCCGTCCTTTTACCCACTC-3'), *Fbn1* (F: 5'-

GGACAGCTCAGCGGGATTG-3', R: 5'- AGGACACATCTCACAGGGGT-3'), *Fn1* (F: 5'-GCTCAGCAAATCGTGCAGC -3', R: 5'- CTAGGTAGGTCCGTTCCCACT -3'), *Col2a1* (F: 5'-GGGAATGTCCTCTGCGATGAC-3', R: 5'-GAAGGGGATCTCGGGGTT-3'), *Col10a1* (F: 5'-TTCTGCTGCTAATGTTCTTGACC-3', R: 5'- GGGATGAAGTATTGTGTCTTGGG-3').

Isolation and differentiation of primary chondrocytes

Primary costal chondrocytes were isolated as described previously[62]. The ribcage of P5 mouse pups was dissected, flattened and soft tissue was removed. The cartilaginous portions of the ribs were then transferred into PBS containing 10× penicillin and streptomycin (Gibco). The ribs were digested with 15 ml pronase (2mg/ml, Sigma-Aldrich) in a 50 ml Falcon tube for 1 h at 37 °C in a tissue culture incubator under a 5% CO_2 atmosphere. The pronase solution was replaced with 15 ml of collagenase D (3 mg/ml, Sigma-Aldrich) followed by incubation for 1 h under the same conditions with gentle agitation every 10 min. After 45 min of incubation, the collagenase D solution was vigorously pipetted up and down over the thoracic cages. The solution was finally transferred into a 50 ml falcon tube. The soft tissue debris was removed as it sediments slower and the process was repeated with sterile PBS buffer. The cleaned cartilage was then digested again with 15 ml collagenase D solution for 4-5 hours at 37 °C in the cell culture incubator. Finally, primary chondrocytes were released by pipetting the solution containing the cartilage fragments up and down ~10 times. This digest was passed through 40 μm cell strainer and pelleted by centrifugation at 300 g for 5 min. The chondrocyte pellet was rinsed twice with PBS and chondrocytes were resuspended in 10 ml complete DMEM medium, plated at a density of $10^5/cm^2$ on 6-well plates and cultured in complete DMEM. Upon reaching confluency, the medium was replaced with chondrocyte maturation medium (complete DMEM supplemented with 50 μg/ml ascorbic acid and 10 mM β-glycerophosphate). The medium was changed every 2 days and mineral deposition was visualized after 21 d by alizarin red staining. For this, the differentiated and matured chondrocytes were rinsed with PBS and fixed with 10% formaldehyde (MP Biomedicals) for 15 minutes at RT. The cell layer was rinsed twice with distilled water and incubated in 1 mL of 40 mM alizarin red staining solution (pH 4.1) per well for 20 min at RT under gentle agitation on a shaker. Plates were incubated at room temperature for 20 minutes with gentle shaking. The alizarin red staining solution was removed

and the wells were rinsed several times with 5 mL of distilled water. Prior to brightfield imaging, excess water was removed and the cell layer was dried at RT. The cell layers were imaged and the stained mineral deposition was quantified using the ImageJ Fiji.

ATAC-seq and transcriptomics analyses of ADAMTS10 and ADAMTS17 expression

Sample generation, ATAC-seq, RNA sequencing and data analyses for the data set have been described recently[42]. No additional human products of conceptions that were not previously described, were used for this manuscript. In brief, epiphyses (long bones) or whole elements (pooled phalanges or metapodials) were micro-dissected and RNA was extracted after tissue homogenization followed by RNA sequencing. For ATAC-seq, tissues were digested with collagenase to generate single cell suspensions, which were then subjected to the ATAC-seq protocol. The data sets for the stylopodial and zeugopodial elements are deposited in the Gene Expression Omnibus repository under the accession numbers GSE252289 (human long bone skeleton ATAC-seq) and GSE252288 (human long bone skeleton RNA-seq). The data sets for the autopodial elements will be published elsewhere (Okamoto & Capellini, manuscript in preparation).

RNAScope in-situ hybridization

WT mouse embryos at E13.5, E16.5, and P0 were fixed in 4% paraformaldehyde in PBS overnight at 4 °C, dehydrated, and embedded in paraffin. Fresh 6 µm sections were used for in-situ hybridization using RNAscope (Advanced Cell Diagnostics) following the manufacturer's protocol. Tissue localization of *Adamts17* mRNA was achieved with a probe recognizing the mRNA from mouse *Adamts17* (#316441) in combination with the RNAscope 2.0 HD detection kit "RED". Tissue sections were counterstained with hematoxylin and cover-slipped with Cytoseal 60 (Electron Microscopy Science). After curation of the mounting medium, sections were observed using an Olympus BX51 upright microscope equipped with a CCD camera (Leica Microsystems) for imaging.

857 **Isolation of primary mouse skin fibroblasts**

858 Mice were euthanized using CO2 inhalation followed by cervical dislocation and skin fibroblasts were
859 isolated using enzymatic digestion. Following euthanasia, the dorsal skin was shaved and 1-2cm2
860 section was excised using sterile scissors and forceps. The excised skin was washed in phosphate-
861 buffered saline (PBS). The skin was minced into 1-2mm2 fragments and transferred into a 50ml conical
862 tube. The tissue was digested using 2mg/ml Collagenase type II (Worthington, LS004202) in DMEM.
863 The tube was incubated at 37oC for 1 hour with gentle agitation to release the fibroblasts. After
864 digestion, the cell suspension was triturated with a 10ml pipette to further dissociate the tissue. The
865 suspension was then filtered through a 70um cell strainer to remove undigested fragments. The
866 filtered cell suspension was centrifuged at 300g for 5 minutes at room temperature. The resulting cell
867 pellet was resuspended in DMEM. The cell suspension was plated onto sterile 10cm culture dishes and
868 incubated at 37oC, 5% CO2. 24h post-plating, the medium was replaced to remove non-adherent cells.

869

870 **N-terminomics via TAILS**

871 For iTRAQ labelling, we co-cultured HDFs with HEK293 cells expressing ADAMTS17 or ADAMTS17-EA (1
872 × 10^6 cells each, two 10 cm dishes). After reaching confluence, the cell layer was rinsed with PBS and
873 phenol-free serum-free DMEM was added. After 2 d and 4 d, the medium was collected and EDTA (10
874 mM final concentration) and one tablet of Complete EDTA-free protease inhibitors (Roche), dissolved
875 in 250 μl water, were added. The medium was cleared of cellular debris by centrifugation at 500 rpm
876 for 5 min, sterile filtrated through a 0.22 μm filter, and stored at -80 °C. Media (~40 ml) were thawed
877 and concentrated to 2.5 mL with centrifugal filter devices (Amicon Ultra-4, 3kDa cut-off; #UFC800324).
878 Proteins were then precipitated by adding 20 mL of ice-cold acetone and 2.5 mL ice cold methanol
879 followed by vortexing and incubation at -80 °C for 3 h. Protein precipitates were collected by
880 centrifugation at 14,200 g in a Beckman JS-13.1 outswing rotor at 4 °C for 20 min. The supernatant was
881 decanted and the protein pellets were air dried. Air-dried pellets were dissolved in 360 μL 8 M
882 guanidine-HCl, 504 μL double-distilled water, and 288 μL 1M HEPES buffer resulting in terminal amine
883 isotopic labeling of substrates (TAILS) buffer (final concentration: 2.5 M GuHCl, 250 mM HEPES, pH7.8).

300 µg of protein from the TS17X1-WT and TS17X1-mut samples were prepared for iTRAQ-TAILS as previously described[63]. In brief, protein was reduced and alkylated with DTT and IAA respectively. Proteins samples were mixed at a 1:1 ratio with iTRAQ labels 113 (TS17X1-WT) or 115 (TS17X1-mut) in DMSO at 37° C overnight and quenched with 1 M tris pH 8. Samples were then combined prior to overnight digestion with trypsin. N-terminally labeled peptides were enriched as previously described using the hyper-dendritic polyglycerol aldehyde[64]. Prior to MS analysis, the samples were desalted using a C18 Ziptip and reconstituted in 50 µL 1% acetic acid. Peptides were identified with a Dionex Ultimate 3000 UHPLC interfaced with a Thermo LTQObitrap Elite hybrid mass spectrometer system. The HPLC column was a Dionex 15 cm x 75 µm id Acclaim Pepmap C18, 2µm, 100 Å reversed- phase capillary chromatography column. 5 µL volumes of the extract were injected and the peptides eluted from the column by an acetonitrile/0.1% formic acid gradient at a flow rate of 0.3 µL/min were introduced into the source of the mass spectrometer on-line operated at 1.9 kV. The digest was analyzed using a data dependent MS method acquiring full scan mass spectra to determine peptide molecular weights and product ion spectra to determine amino acid sequence in successive instrument scans. Both collision-induced dissociation (CID) and higher-energy collisional dissociation (HCD) fragmentation methods were performed on the top-8 most abundant precursor ions in each scan cycle. HCD fragmentation is required to quantify the reporter ions of the iTRAQ labels on peptides. The samples were analyzed using a data dependent acquisition (DDA) using both HCD and CID fragmentations. The resulting data were searched using Sequest program which integrated in Proteomics Discoverer 2.5 software package against Uni-prot human protein sequence database (March, 2024). Trypsin (semi) was set as protease, carbomidomethylation of Cys was set as a static modification and iTRAQ 8-plex of peptide N-terminal, Lys and Tyr, oxidation of Met, and N-term Gln cyclization were set as dynamic modifications.

Yeast-2-hybrid screening

An ULTImate Y2H SCREEN was performed by Hybrigenics Services using ADAMTS17-AD (aa 546-1122) as bait together with the Prey Library Human Placenta_RP6. The bait was cloned into the pB27 (N-LexA-bait-C fusion) vector. 60 clones were processed and 170 million interactions analyzed.

Statistical analyses

Statistical analyses were performed using the OriginPro 2018 software. N=2 samples were compared with a two-sided Student's t-test and n≥3 samples with a one-sided ANOVA. P-values <0.05 were considered statistically different.

Author contributions

NT, SZK, ZB, LWW, BBW and DRM, performed experiments and analyzed data. SSA and DH analyzed data and contributed to study design. DR, ASO, TDC analyzed ATAC-seq and transcriptomics data. DH conceptualized the study, performed experiments, analyzed data, drafted the manuscript and prepared the figures. All authors edited the manuscript and figures and approved the final version.

Acknowledgements

This research was in part supported by a grant from the National Institutes of Health (R01AR070748 to D.H.). We thank Dr. Dieter Reinhardt (McGill University, Montreal, Canada) for kindly providing the fibrillin-1 antibody and the V5-tagged rFN1 expression plasmid. We thank Damien Laudier (Orthopedic Research Laboratories, Icahn School of Medicine at Mount Sinai, New York, NY) for growth plate and skin histology.

Data Availability

The data sets for the stylopodial and zeugopodial elements are deposited in the Gene Expression Omnibus repository under the accession numbers GSE252289 (human long bone skeleton ATAC-seq) and GSE252288 (human long bone skeleton RNA-seq). The data sets for the autopodial elements will be published elsewhere (Okamoto & Capellini, manuscript in preparation) and made publicly available.

Conflict of Interest

The authors declare no financial or non-financial conflict of interest.

References

1 Stanley, S., Balic, Z. & Hubmacher, D. Acromelic dysplasias: how rare musculoskeletal disorders reveal biological functions of extracellular matrix proteins. *Ann. N. Y. Acad. Sci.*, doi:10.1111/nyas.14465 (2020).

2 Le Goff, C. & Cormier-Daire, V. Genetic and molecular aspects of acromelic dysplasia. *Pediatr Endocrinol Rev* **6**, 418-423 (2009).

3 Marzin, P. *et al.* Weill-Marchesani syndrome: natural history and genotype-phenotype correlations from 18 news cases and review of literature. *J. Med. Genet.*, doi:10.1136/jmg-2023-109288 (2023).

4 Morales, J. *et al.* Homozygous mutations in ADAMTS10 and ADAMTS17 cause lenticular myopia, ectopia lentis, glaucoma, spherophakia, and short stature. *Am. J. Hum. Genet.* **85**, 558-568, doi:10.1016/j.ajhg.2009.09.011 (2009).

5 Kutz, W. E. *et al.* Functional analysis of an ADAMTS10 signal peptide mutation in Weill-Marchesani syndrome demonstrates a long-range effect on secretion of the full-length enzyme. *Hum. Mutat.* **29**, 1425-1434, doi:10.1002/humu.20797 (2008).

6 Dagoneau, N. *et al.* ADAMTS10 mutations in autosomal recessive Weill-Marchesani syndrome. *Am. J. Hum. Genet.* **75**, 801-806, doi:10.1086/425231 (2004).

7 Haji-Seyed-Javadi, R. *et al.* LTBP2 mutations cause Weill-Marchesani and Weill-Marchesani-like syndrome and affect disruptions in the extracellular matrix. *Hum. Mutat.* **33**, 1182-1187, doi:10.1002/humu.22105 (2012).

8 Cecchi, A. *et al.* Missense mutations in FBN1 exons 41 and 42 cause Weill-Marchesani syndrome with thoracic aortic disease and Marfan syndrome. *American journal of medical genetics. Part A* **161A**, 2305-2310, doi:10.1002/ajmg.a.36044 (2013).

9 Faivre, L. *et al.* In frame fibrillin-1 gene deletion in autosomal dominant Weill-Marchesani syndrome. *J. Med. Genet.* **40**, 34-36, doi:10.1136/jmg.40.1.34 (2003).

10 Karoulias, S. Z. *et al.* A novel ADAMTS17 variant that causes Weill-Marchesani syndrome 4 alters fibrillin-1 and collagen type I deposition in the extracellular matrix. *Matrix Biol.* **88**, 1-18, doi:10.1016/j.matbio.2019.11.001 (2020).

11 Evans, D. R. *et al.* A novel pathogenic missense ADAMTS17 variant that impairs secretion causes Weill-Marchesani Syndrome with variably dysmorphic hand features. *Sci Rep* **10**, 10827, doi:10.1038/s41598-020-66978-8 (2020).

12 Faivre, L. *et al.* Clinical homogeneity and genetic heterogeneity in Weill-Marchesani syndrome. *American journal of medical genetics. Part A* **123A**, 204-207, doi:10.1002/ajmg.a.20289 (2003).

13 Kuchtey, J. *et al.* Screening ADAMTS10 in Dog Populations Supports Gly661Arg as the Glaucoma-Causing Variant in Beagles. *Invest Ophth Vis Sci* **54**, 1881-1886, doi:10.1167/iovs.12-10796 (2013).

14 Kuchtey, J. *et al.* Mapping of the disease locus and identification of ADAMTS10 as a candidate gene in a canine model of primary open angle glaucoma. *PLoS genetics* **7**, e1001306, doi:10.1371/journal.pgen.1001306 (2011).

15 Oliver, J. A., Forman, O. P., Pettitt, L. & Mellersh, C. S. Two Independent Mutations in ADAMTS17 Are Associated with Primary Open Angle Glaucoma in the Basset Hound and Basset Fauve de Bretagne Breeds of Dog. *PloS one* **10**, e0140436, doi:10.1371/journal.pone.0140436 (2015).

16 Gould, D. *et al.* ADAMTS17 mutation associated with primary lens luxation is widespread among breeds. *Vet Ophthalmol* **14**, 378-384, doi:10.1111/j.1463-5224.2011.00892.x (2011).

17 Farias, F. H. *et al.* An ADAMTS17 splice donor site mutation in dogs with primary lens luxation. *Invest. Ophthalmol. Vis. Sci.* **51**, 4716-4721, doi:10.1167/iovs.09-5142 (2010).

18 Jeanes, E. C., Oliver, J. A. C., Ricketts, S. L., Gould, D. J. & Mellersh, C. S. Glaucoma-causing ADAMTS17 mutations are also reproducibly associated with height in two domestic dog breeds: selection for short stature may have contributed to increased prevalence of glaucoma. *Canine Genet Epidemiol* **6**, 5, doi:10.1186/s40575-019-0071-6 (2019).

19 Karoulias, S. Z., Taye, N., Stanley, S. & Hubmacher, D. The ADAMTS/Fibrillin Connection: Insights into the Biological Functions of ADAMTS10 and ADAMTS17 and Their Respective Sister Proteases. *Biomolecules* **10**, doi:10.3390/biom10040596 (2020).

20 Hubmacher, D. & Apte, S. S. Genetic and functional linkage between ADAMTS superfamily proteins and fibrillin-1: a novel mechanism influencing microfibril assembly and function. *Cell. Mol. Life Sci.* **68**, 3137-3148, doi:10.1007/s00018-011-0780-9 (2011).

21 Kutz, W. E. *et al.* ADAMTS10 protein interacts with fibrillin-1 and promotes its deposition in extracellular matrix of cultured fibroblasts. *J. Biol. Chem.* **286**, 17156-17167, doi:10.1074/jbc.M111.231571 (2011).

22 Hubmacher, D. *et al.* Unusual life cycle and impact on microfibril assembly of ADAMTS17, a secreted metalloprotease mutated in genetic eye disease. *Sci. Rep.* **7**, 41871, doi:10.1038/srep41871 (2017).

23 Satz-Jacobowitz, B. & Hubmacher, D. The quest for substrates and binding partners: A critical barrier for understanding the role of ADAMTS proteases in musculoskeletal development and disease. *Dev. Dyn.* **250**, 8-26, doi:10.1002/dvdy.248 (2021).

24 Apte, S. S. ADAMTS Proteins: Concepts, Challenges, and Prospects. *Methods Mol. Biol.* **2043**, 1-12, doi:10.1007/978-1-4939-9698-8_1 (2020).

25 Mead, T. J. & Apte, S. S. ADAMTS proteins in human disorders. *Matrix Biol.* **71-72**, 225-239, doi:10.1016/j.matbio.2018.06.002 (2018).

26 Santamaria, S. ADAMTS-5: A difficult teenager turning 20. *Int. J. Exp. Pathol.* **101**, 4-20, doi:10.1111/iep.12344 (2020).

27 Longpre, J. M. *et al.* Characterization of proADAMTS5 processing by proprotein convertases. *Int. J. Biochem. Cell Biol.* **41**, 1116-1126, doi:10.1016/j.biocel.2008.10.008 (2009).

28 Koo, B. H. *et al.* Regulation of ADAMTS9 secretion and enzymatic activity by its propeptide. *J. Biol. Chem.* **282**, 16146-16154, doi:10.1074/jbc.M610161200 (2007).

29 Koo, B. H. *et al.* Cell-surface processing of pro-ADAMTS9 by furin. *J. Biol. Chem.* **281**, 12485-12494, doi:10.1074/jbc.M511083200 (2006).

30 Wang, P. *et al.* Proprotein convertase furin interacts with and cleaves pro-ADAMTS4 (Aggrecanase-1) in the trans-Golgi network. *J. Biol. Chem.* **279**, 15434-15440, doi:10.1074/jbc.M312797200 (2004).

31 Wang, L. W. *et al.* Adamts10 inactivation in mice leads to persistence of ocular microfibrils subsequent to reduced fibrillin-2 cleavage. *Matrix Biol.* **77**, 117-128, doi:10.1016/j.matbio.2018.09.004 (2019).

32 Balic, Z. *et al.* Alternative splicing of the metalloprotease ADAMTS17 spacer regulates secretion and modulates autoproteolytic activity. *FASEB J.* **35**, e21310, doi:10.1096/fj.202001120RR (2021).

33 Oichi, T. *et al.* Adamts17 is involved in skeletogenesis through modulation of BMP-Smad1/5/8 pathway. *Cell. Mol. Life Sci.*, doi:10.1007/s00018-019-03188-0 (2019).

34 Mularczyk, E. J. *et al.* ADAMTS10-mediated tissue disruption in Weill-Marchesani syndrome. *Hum. Mol. Genet.* **27**, 3675-3687, doi:10.1093/hmg/ddy276 (2018).

35 Wu, H. J., Mortlock, D. P., Kuchtey, R. W. & Kuchtey, J. Altered Ocular Fibrillin Microfibril Composition in Mice With a Glaucoma-Causing Mutation of Adamts10. *Invest. Ophthalmol. Vis. Sci.* **62**, 26, doi:10.1167/iovs.62.10.26 (2021).

36 Hubmacher, D. *et al.* Limb- and tendon-specific Adamtsl2 deletion identifies a role for ADAMTSL2 in tendon growth in a mouse model for geleophysic dysplasia. *Matrix Biol.* **82**, 38-53, doi:10.1016/j.matbio.2019.02.001 (2019).

37 Breur, G. J., VanEnkevort, B. A., Farnum, C. E. & Wilsman, N. J. Linear relationship between the volume of hypertrophic chondrocytes and the rate of longitudinal bone growth in growth plates. *J. Orthop. Res.* **9**, 348-359, doi:10.1002/jor.1100090306 (1991).

38 Kember, N. F. Comparative patterns of cell division in epiphyseal cartilage plates in the rat. *J. Anat.* **111**, 137-142 (1972).

39 Dy, P. *et al.* Sox9 directs hypertrophic maturation and blocks osteoblast differentiation of growth plate chondrocytes. *Dev. Cell* **22**, 597-609, doi:10.1016/j.devcel.2011.12.024 (2012).

40 Kozhemyakina, E., Cohen, T., Yao, T. P. & Lassar, A. B. Parathyroid hormone-related peptide represses chondrocyte hypertrophy through a protein phosphatase 2A/histone deacetylase 4/MEF2 pathway. *Mol. Cell. Biol.* **29**, 5751-5762, doi:10.1128/MCB.00415-09 (2009).

41 Sabatier, L. *et al.* Fibrillin assembly requires fibronectin. *Mol. Biol. Cell* **20**, 846-858, doi:10.1091/mbc.E08-08-0830 (2009).

42 Richard, D. *et al.* Functional genomics of human skeletal development and the patterning of height heritability. *Cell*, doi:10.1016/j.cell.2024.10.040 (2024).

43 Dreos, R., Ambrosini, G., Groux, R., Cavin Perier, R. & Bucher, P. The eukaryotic promoter database in its 30th year: focus on non-vertebrate organisms. *Nucleic Acids Res.* **45**, D51-D55, doi:10.1093/nar/gkw1069 (2017).

44 Rezza, A. *et al.* Signaling Networks among Stem Cell Precursors, Transit-Amplifying Progenitors, and their Niche in Developing Hair Follicles. *Cell reports* **14**, 3001-3018, doi:10.1016/j.celrep.2016.02.078 (2016).

45 Sennett, R. *et al.* An Integrated Transcriptome Atlas of Embryonic Hair Follicle Progenitors, Their Niche, and the Developing Skin. *Dev. Cell* **34**, 577-591, doi:10.1016/j.devcel.2015.06.023 (2015).

46 Marzin, P., Cormier-Daire, V. & Tsilou, E. in *GeneReviews((R))* (eds M. P. Adam *et al.*) (1993).

47 Cooper, K. L. *et al.* Multiple phases of chondrocyte enlargement underlie differences in skeletal proportions. *Nature* **495**, 375-378, doi:10.1038/nature11940 (2013).

48 Wilsman, N. J., Farnum, C. E., Leiferman, E. M., Fry, M. & Barreto, C. Differential growth by growth plates as a function of multiple parameters of chondrocytic kinetics. *J. Orthop. Res.* **14**, 927-936, doi:10.1002/jor.1100140613 (1996).

49 Wilsman, N. J., Farnum, C. E., Green, E. M., Lieferman, E. M. & Clayton, M. K. Cell cycle analysis of proliferative zone chondrocytes in growth plates elongating at different rates. *J. Orthop. Res.* **14**, 562-572, doi:10.1002/jor.1100140410 (1996).

50 Kennedy, A. M. *et al.* MMP13 mutation causes spondyloepimetaphyseal dysplasia, Missouri type (SEMD(MO). *J. Clin. Invest.* **115**, 2832-2842, doi:10.1172/JCI22900 (2005).

51 Inada, M. *et al.* Critical roles for collagenase-3 (Mmp13) in development of growth plate cartilage and in endochondral ossification. *Proc Natl Acad Sci U S A* **101**, 17192-17197, doi:10.1073/pnas.0407788101 (2004).

52 Vu, T. H. *et al.* MMP-9/gelatinase B is a key regulator of growth plate angiogenesis and apoptosis of hypertrophic chondrocytes. *Cell* **93**, 411-422, doi:10.1016/s0092-8674(00)81169-1 (1998).

53 Knauper, V. *et al.* Cellular activation of proMMP-13 by MT1-MMP depends on the C-terminal domain of MMP-13. *FEBS Lett.* **532**, 127-130, doi:10.1016/s0014-5793(02)03654-2 (2002).

54 Wohl, A. P., Troilo, H., Collins, R. F., Baldock, C. & Sengle, G. Extracellular Regulation of Bone Morphogenetic Protein Activity by the Microfibril Component Fibrillin-1. *J. Biol. Chem.* **291**, 12732-12746, doi:10.1074/jbc.M115.704734 (2016).

55 Sengle, G. *et al.* Targeting of bone morphogenetic protein growth factor complexes to fibrillin. *J. Biol. Chem.* **283**, 13874-13888, doi:10.1074/jbc.M707820200 (2008).

56 Sabatier, L. *et al.* Complex contributions of fibronectin to initiation and maturation of microfibrils. *Biochem. J.* **456**, 283-295, doi:10.1042/BJ20130699 (2013).

57 Schindelin, J., Rueden, C. T., Hiner, M. C. & Eliceiri, K. W. The ImageJ ecosystem: An open platform for biomedical image analysis. *Mol. Reprod. Dev.* **82**, 518-529, doi:10.1002/mrd.22489 (2015).

58 Schindelin, J. *et al.* Fiji: an open-source platform for biological-image analysis. *Nat. Methods* **9**, 676-682, doi:10.1038/nmeth.2019 (2012).

59 Lee, C. S. *et al.* Mutations in Fibronectin Cause a Subtype of Spondylometaphyseal Dysplasia with "Corner Fractures". *Am. J. Hum. Genet.* **101**, 815-823, doi:10.1016/j.ajhg.2017.09.019 (2017).

60 Reznikoff, C. A., Bertram, J. S., Brankow, D. W. & Heidelberger, C. Quantitative and qualitative studies of chemical transformation of cloned C3H mouse embryo cells sensitive to postconfluence inhibition of cell division. *Cancer Res.* **33**, 3239-3249 (1973).

61 Reznikoff, C. A., Brankow, D. W. & Heidelberger, C. Establishment and characterization of a cloned line of C3H mouse embryo cells sensitive to postconfluence inhibition of division. *Cancer Res.* **33**, 3231-3238 (1973).

62 Mirando, A. J., Dong, Y., Kim, J. & Hilton, M. J. Isolation and culture of murine primary chondrocytes. *Methods Mol. Biol.* **1130**, 267-277, doi:10.1007/978-1-62703-989-5_20 (2014).

63 Martin, D. R. *et al.* Proteomics identifies a convergent innate response to infective endocarditis and extensive proteolysis in vegetation components. *JCI Insight* **5**, doi:10.1172/jci.insight.135317 (2020).

64 Nandadasa, S. *et al.* Degradomic Identification of Membrane Type 1-Matrix Metalloproteinase as an ADAMTS9 and ADAMTS20 Substrate. *Mol Cell Proteomics* **22**, 100566, doi:10.1016/j.mcpro.2023.100566 (2023).

Table 1: Accessible genomic regions in *ADAMTS10* in cartilage as determined by ATAC-seq.

Gene	Start	End	Skeletal elements
ADAMTS10 **(chr19)**	8483730	8486836	Hand Phalanx II; Metacarpal IV
	8504872	8509348	Foot Phalanges I-V; Metatarsals II-V; Hand Phalanges I-V; Metacarpals I-V
	8576228	8582004	Foot Phalanges II-V; Metatarsals II-V; Hand Phalanges I-V; Metacarpals I-V
	8584785	8586747	Metacarpal IV
	8590420	8597323	Distal & Proximal Femur; Distal & Proximal Humerus; Distal & Proximal Radius; Distal & Proximal Tibia; Foot Phalanges I-V; Metatarsals II-V; Hand Phalanges I-V; Metacarpals I-V
	8606826	8611019	Distal & Proximal Femur; Distal & Proximal Humerus; Distal & Proximal Radius; Distal & Proximal Tibia; Foot Phalanges I-V; Metatarsals I-V; Hand Phalanges I-V; Metacarpals I-V
	8611370	8614416	Foot Phalanges I, II, IV, V; Metatarsals II, III, V; Hand Phalanges I-V; Metacarpals I-V
	8614566	8615966	Metacarpal II, III
	8637955	8639246	Metacarpal II, III
	8654156	8656442	Metatarsal III; Hand Phalanx V; Metacarpals II, III, V

The start and end sites of the open chromatin regions were mapped to chromosome 19 (*ADAMTS10*) based on human genome assembly GRCh38 (hg38).

1101 **Table 2: Accessible genomic regions in *ADAMTS17* in cartilage as determined by ATAC-seq.**

Gene	Start	End	Skeletal elements
ADAMTS17 **(chr15)**	99950945	99953010	Foot Phalanges II-V; Metatarsals I-V; Hand Phalanges III-V; Metacarpals II-V
	99957622	99960241	Foot Phalanges I-III, V; Metatarsals I-V; Hand Phalanges I, III, IV, V; Metacarpals I-III, V
	99980194	99985410	Foot Phalanges I-III, V; Metatarsals I, II, V; Hand Phalanges III, V; Metacarpals II, III, V
	100007670	100009415	Foot Phalanx II; Metatarsal II; Hand Phalanx IV; Metacarpals II, V;
	100018494	100022360	Foot Phalanges I-III, V; Metatarsals I-III, V; Hand Phalanges I, III, IV, V; Metacarpals II, III
	100032576	100033757	Metatarsal V
	100042238	100044322	Foot Phalanges I-V; Metatarsals I-V; Hand Phalanges I-V; Metacarpals I-V
	100058266	100062127	Foot Phalanges I-V; Metatarsals I-V; Hand Phalanges I-V; Metacarpals I-V
	100103369	100105117	Foot Phalanges I-V; Hand Phalanges I-V
	100110533	100116846	Foot Phalanges I-V; Metatarsals I-V; Hand Phalanges I-V; Metacarpals I-V
	100124861	100126574	Foot Phalanx I; Metatarsal II; Hand Phalanx III; Metacarpals II, III
	100131195	100133136	Foot Phalanges I, II; Metatarsals I-V; Hand Phalanges I-V; Metacarpals I-V
	100140773	100142360	Foot Phalanges I, II; Metatarsals I, II, IV, V; Hand Phalanges I, II, V; Metacarpals I-III, V
	100196165	100197462	Foot Phalanges III, V; Metatarsals I, IV, V; Hand Phalanges I, III, IV, V; Metacarpals I-III, V
	100199818	100203168	Foot Phalanges I-V; Metatarsals II-V; Hand Phalanges I-V; Metacarpals I-V
	100224224	100226042	Metatarsals III-V; Hand Phalanx V; Metacarpals II-V
	100234080	100236829	Metacarpal II, IV, V
	100241067	100243238	Distal & Proximal Femur; Proximal Humerus; Distal & Proximal Radius; Proximal Tibia; Foot Phalanges I, V; Metatarsals I-V; Hand Phalanx I-V; Metacarpals I-IV
	100264745	100266902	Foot Phalanges I, II; Metatarsals I, II, IV, V; Metacarpal V
	100307139	100312190	Distal & Proximal Femur; Distal & Proximal Humerus; Proximal Radius; Proximal Tibia; Foot Phalanges I, II; Metatarsals I, II, IV, V; Hand Phalanx V; Metacarpals II-IV
	100331806	100332722	Metatarsal V
	100338262	100340520	Distal Femur; Foot Phalanges I, II, V; Metatarsals I-V; Hand Phalanges I-V; Metacarpals II, III, V
	100372584	100374300	Distal Femur; Distal Humerus; Foot Phalanges I-III, V; Metatarsals I-V; Hand Phalanges I, II, IV, V; Metacarpals I-V

1102

1103 The start and end positions of the open chromatin regions were mapped chromosome 15 (*ADAMTS17*) based on human
1104 genome assembly GRCh38 (hg38).

1105

1106